CrossMark

Signatures of *r*-process Enrichment in Supernovae from Collapsars

Jennifer Barnes[1] and Brian D. Metzger[2,3]
[1] Kavli Institute for Theoretical Physics, Kohn Hall, University of California, Santa Barbara, CA 93106, USA; jlbarnes@kitp.ucsb.edu
[2] Department of Physics and Columbia Astrophysics Laboratory, Columbia University, New York, NY 10027, USA
[3] Center for Computational Astrophysics, Flatiron Institute, 162 5th Ave., New York, NY 10010, USA

Abstract

Despite recent progress, the astrophysical channels responsible for rapid neutron capture (*r*-process) nucleosynthesis remain an unsettled question. Observations of the kilonova following the gravitational-wave-detected neutron star merger GW170817 established mergers as one site of the *r*-process, but additional sources may be needed to fully explain *r*-process enrichment in the universe. One intriguing possibility is that rapidly rotating massive stars undergoing core collapse launch *r*-process-rich outflows off the accretion disks formed from their infalling matter. In this scenario, *r*-process winds are one component of the supernova (SN) ejecta produced by "collapsar" explosions. We present the first systematic study of the effects of *r*-process enrichment on the emission from collapsar-generated SNe. We semianalytically model *r*-process SN emission from explosion out to late times and determine its distinguishing features. The ease with which *r*-process SNe can be identified depends on how effectively wind material mixes into the initially *r*-process-free outer layers of the ejecta. In many cases, enrichment produces a near-infrared (NIR) excess that can be detected within ∼75 days of explosion. We also discuss optimal targets and observing strategies for testing the *r*-process collapsar theory, and find that frequent monitoring of optical and NIR emission from high-velocity SNe in the first few months after explosion offers a reasonable chance of success while respecting finite observing resources. Such early identification of *r*-process collapsar candidates also lays the foundation for nebular-phase spectroscopic follow-up in the NIR and mid-infrared, for example, with the James Webb Space Telescope.

1. Introduction

The astrophysical site—or sites—of rapid neutron capture (*r*-process) nucleosynthesis, which produces roughly half of all elements more massive than iron (Burbidge et al. 1957; Cameron 1957), remains a major outstanding question in astrophysics (see Horowitz et al. 2019; Thielemann et al. 2020; Cowan et al. 2021, for recent reviews).

The association of a radioactively powered kilonova (henceforth kn170817; Abbott et al. 2017a; Arcavi et al. 2017; Coulter et al. 2017; Drout et al. 2017; Evans et al. 2017; Kilpatrick et al. 2017; McCully et al. 2017; Nicholl et al. 2017; Shappee et al. 2017; Smartt et al. 2017; Soares-Santos et al. 2017; Kasliwal et al. 2022) with the gravitational-wave-detected neutron star merger (NSM) GW170817 (Abbott et al. 2017c) represented a watershed in the understanding of *r*-process origins. In addition to demonstrating the long-theorized viability of NSMs as *r*-process sites (e.g., Lattimer & Schramm 1974; Symbalisty & Schramm 1982; Eichler et al. 1989; Freiburghaus et al. 1999), kn170817 provided an unprecedentedly detailed picture of the various environments in which the *r*-process may occur following a merger (Cowperthwaite et al. 2017; Drout et al. 2017; Kilpatrick et al. 2017; Tanvir et al. 2017, among others). In particular, spectral analysis (e.g., Chornock et al. 2017; Kasen et al. 2017; Tanaka et al. 2017; see Siegel 2019; Barnes 2020, for reviews) pointed to accretion disk outflows (Metzger et al. 2008; Fernández & Metzger 2013; Perego et al. 2014; Just et al. 2015; Siegel & Metzger 2017; Fujibayashi et al. 2018;

Fernández et al. 2019) as the locus of the heaviest element production. (However, see Waxman et al. 2018 for an alternative interpretation.)

Despite this success, the idea that NSMs are the sole *r*-process sources in the universe may be in tension with lines of evidence that call for *r*-production in events with comparatively short delay times relative to star formation (Côté et al. 2019; Siegel et al. 2019; Zevin et al. 2019; van de Voort et al. 2020; Jeon et al. 2021; Molero et al. 2021; de los Reyes et al. 2022) or kick velocities lower than the escape velocities of their sometimes diminutive host galaxies (e.g., Beniamini et al. 2016; Ji et al. 2016). Some recent Galactic chemical evolution studies (Tsujimoto 2021; Naidu et al. 2022) have argued for two distinct *r*-process sources (though see Beniamini et al. 2018; Duggan et al. 2018; Bartos & Márka 2019; Macias & Ramirez-Ruiz 2019; Schönrich & Weinberg 2019; Fraser & Schonrich 2022). These clues hint that core-collapse supernovae (CCSNe) may contribute as an additional *r*-process site.

Though CCSNe were nominated as *r*-process sites as soon as the nuclear physics of the *r*-process was understood (Burbidge et al. 1957), decades of incremental progress culminated in the finding (e.g., Qian & Woosley 1996; Hoffman et al. 1997; Meyer & Brown 1997; Thompson et al. 2001) that matter ablated from a newly formed neutron star (NS) cannot in most cases achieve the combination of entropy and neutron-richness required for a successful *r*-process. (Such proto-NS winds may still generate lighter neutron- or proton-rich nuclei; e.g., Fröhlich et al. 2006; Arcones & Montes 2011.)

More recent explorations have focused on rarer SN subtypes, such as explosions that leave behind very rapidly spinning (Burrows et al. 2007) and/or highly magnetized NSs (Thompson et al. 2004; Metzger et al. 2007) and their

concomitant "jet-driven" SN explosions (Winteler et al. 2012; Mosta et al. 2014; Mösta et al. 2018; Kuroda et al. 2020), in which the prompt advection of neutron-rich material away from the proto-NS surface avoids the problem of charged current interactions—neutrino capture and e^+/e^- pair creation and capture—that in the absence of rapid expansion thwart the r-process by protonizing the outflowing matter. However, 3D magnetohydrodynamic (MHD) simulations of the explosions (Halevi & Mosta 2018) cast doubt as to whether sufficiently rapid expansion can in fact be realized.

Regardless, MHD SNe and the energetic processes that occur in their immediate aftermath may nevertheless be important for r-production. Broad-lined Type Ic SNe (SNe Ic-BL) are the most obvious by-products of MHD-driven explosions, with kinetic energies ($E_k \sim 10^{52}$ erg; Maeda et al. 2002; Mazzali et al. 2002; Maeda et al. 2003; Mazzali et al. 2003) far exceeding what can be supplied by the standard neutrino mechanism (Scheck et al. 2006; Bruenn et al. 2016; Müller et al. 2017; see Janka et al. 2016, for a review). Some (possibly all) SNe Ic-BL occur in conjunction with long gamma-ray bursts (GRBs; Galama et al. 1998; Bloom et al. 2002; Hjorth et al. 2003; Stanek et al. 2003; Woosley & Bloom 2006). These ultrarelativistic jets may be powered by accretion onto a central compact object (Aloy et al. 2000; Bromberg & Tchekhovskoy 2016; Gottlieb et al. 2022) and serve as indirect evidence for accretion flows with properties akin to those that give rise to the shorter-duration (but otherwise similar) GRBs (Nakar 2007; Berger 2014) associated with NSMs (Abbott et al. 2017b; Goldstein et al. 2017).

The term "collapsar" (e.g., MacFadyen & Woosley 1999) refers to a model for the production of long GRBs/SNe Ic-BL in which the large angular momentum in the outer layers of a rapidly rotating massive star allows material from those layers to circularize and form an accretion disk as the star undergoes core collapse. Recent simulations of collapsar disks (Siegel et al. 2019, hereafter SBM19) found that material in the disk becomes neutron-rich through weak interactions (Beloborodov 2003) and that winds launched from the disk retain a sufficiently low electron fraction to support an r-process. (However, studies adopting different neutrino transport methods do not always find production of the heaviest r-process nuclei, at least not during epochs in the disk evolution when neutrino self-irradiation of the disk outflows is most important. See, e.g., Surman & McLaughlin 2004; Miller et al. 2020; Just et al. 2022.)

The results of SBM19 identify hyperenergetic GRB-SNe and SNe Ic-BL as the SNe most likely to produce an r-process via accretion disk outflows. However, outstanding questions about the engines powering SNe with kinetic energies beyond 10^{51} ergs (which are difficult to explain with the standard neutrino mechanism; e.g., Janka et al. 2016) leave open the possibility that a central engine enables the synthesis of r-process elements even in SNe of somewhat lower energies. The potential for r-production in CCSNe motivates direct searches for its presence in SN light curves and spectra. The signatures of r-process enrichment in SNe will depend sensitively on the quantity of r-process material synthesized and its distribution within the ejecta. Outflows of r-process-rich matter from a collapsar accretion disk may occur at a delay relative to the initial explosion that unbinds the star's outer layers if, for example, accretion rates onto the disk are initially too low to support an r-process (SBM19). This scenario implies an inner core of r-process products deposited behind an outer layer composed of ordinary stellar material (e.g., carbon and oxygen) and radioactive ^{56}Ni synthesized in the explosion. Radiation transport simulations by SBM19 found that such an ejecta structure produced light curves and spectra fairly consistent with observed SNe Ic-BL.

However, even if collapsar disks release an r-process wind into the already-expanding SN ejecta, various processes, such as hydrodynamic instabilities at the wind-ejecta interface, may mix r-process elements out to higher mass coordinates. However, the extent of the mixing is largely unconstrained and may vary among events. While SBM19 found that a fully mixed model could not reproduce emission from SNe Ic-BL, they did not consider intermediate levels of mixing, in which some but not all of the initially r-process-free ejecta from the prompt explosion becomes enriched with r-process material.

In the present work, we use analytic reasoning and semi-analytic modeling to improve on SBM19, extending their analysis to a much broader region of parameter space and investigating the possibility that signs of r-production can be detected directly in the emission of r-process-enriched CCSNe (rCCSNe). In Section 2, we apply simple analytic arguments to establish baseline expectations for the strength of the r-process signal and the timescales on which it may appear. A more detailed rCCSN emission model is developed in Section 3. We validate the model against SNe Ic with typical ($\mathcal{O}(10^{51})$ erg) energies and—we assume—negligible r-process production, before extending it to enriched cases and exploring how the addition of r-process material impacts the SN's light-curve and color evolution. In Section 4, we consider a broad suite of models and discuss the prospects for constraining collapsar r-process production as a function of observational SN properties. We present our conclusions in Section 5.

2. Analytic Considerations

Before proceeding to more detailed SN emission models (Section 3), we present simple analytic arguments to build intuition and illustrate the key factors that determine how easily signs of r-process enrichment can be observed. Here, as in later sections, we model the rCCSN ejecta as a spherical outflow consisting of an r-process-enriched core and an r-process-free envelope. The ejecta has a total mass M_{ej}, which includes some amount of r-process elements, whose mass M_{rp} is concentrated in a core of mass $M_{mix} \geqslant M_{rp}$. Generally, we express the mass of the core as a fraction of M_{ej}. This fraction is henceforth referred to as the *mixing coordinate* and is denoted ψ_{mix}. By definition, $M_{rp}/M_{ej} \leqslant \psi_{mix} \equiv M_{mix}/M_{ej} \leqslant 1.0$. In other words, ψ_{mix} is the normalized interior mass coordinate of the r-process-element-containing core. An illustration of the model is provided in Figure 1, and a summary of its parameters can be found in Table 1, though some of the parameters defined are relevant only for more complex iterations of the model developed in later sections.

Motivated by models of both regular (Yoon et al. 2019) and broad-lined (Taddia et al. 2019) SNe Ic that find evidence of ^{56}Ni mixing out to high velocities, we assume that ^{56}Ni is distributed evenly throughout the ejecta. In Sections 2.1 and 2.2, we ignore r-process decay and treat ^{56}Ni/Co as the sole source of radioactive heating. (We retire this simplification in later sections, since the fraction of energy due to r-process decay increases with time and can be nonnegligible depending on the relative masses of ^{56}Ni and r-process elements; SBM19.)
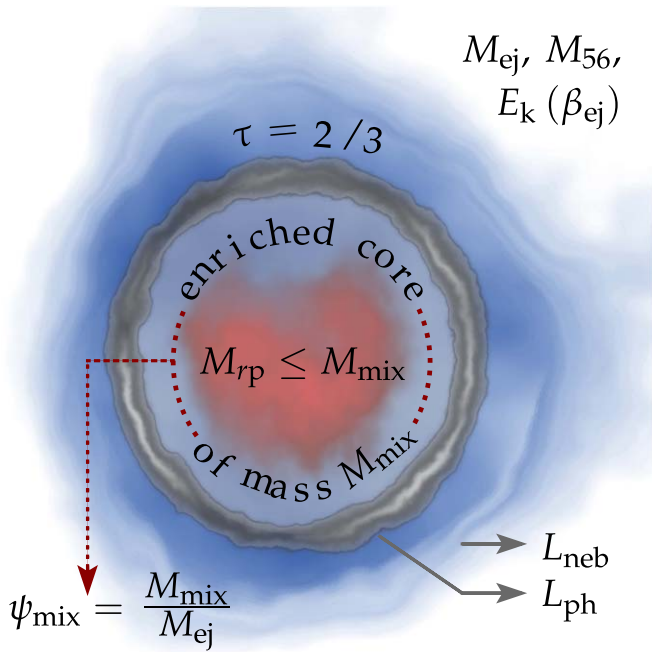
Figure 1. A schematic illustration of our r-process collapsar model, with the main model parameters and emission components highlighted. All models are defined by their total mass, M_{ej}, and kinetic energy, E_k (which together define a characteristic velocity β_{ej}), as well as a ^{56}Ni mass, M_{56}. For the r-process-enriched models, a central core of mass $M_{mix} \leqslant M_{ej}$ is defined, and some mass $M_{rp} \leqslant M_{mix}$ within that core is presumed to be composed of r-process elements. The mixing coordinate ψ_{mix} is the ratio of M_{mix} to M_{ej}. The photosphere, defined as the surface at which $\tau = 2/3$, separates the optically thick and optically thin regions. Emission from the optically thick layers inside the photosphere takes the form of a blackbody, in contrast to emission from the optically thin (nebular) layers.

We first consider r-process signatures during the nebular phase, before moving on to the earlier photospheric phase.

2.1. Nebular Phase

Very late-time observations have been suggested (SBM19) as a key strategy for testing the r-process collapsar hypothesis, since by the nebular phase the ejecta is transparent and lines of sight extend into the inner regions where, for core-envelope models of rCCSNe, the r-process material resides. However, even in the nebular phase, the strength of the signal depends on the degree to which the nebular spectrum of the r-process-rich layers diverges from that of the r-process-free envelope, as well as on the brightness of each component.

In the case of a completely optically thin ejecta heated by uniformly distributed radioactive ^{56}Ni/Co, the ratio of luminosities from the r-process-rich and r-process-free layers is simply $L_{neb}^{rp}/L_{neb}^{sn} = \psi_{mix}/(1 - \psi_{mix})$. (Since we are ignoring heating from r-process decay, this estimate is a conservative lower limit.)

We assign to the r-process-free envelope a spectral energy distribution (SED) derived from late-time photometry of the SN Ic SN 2007gr (Hunter et al. 2009; Bianco et al. 2014), one of the few SNe Ic observed up to ~ 150 days after peak in both optical and near-infrared (NIR) bands. We assume that the r-process-enriched layers shine like a blackbody regardless of the r-process mass fraction in the core. (Thus, the models of Section 2.1 depend only on ψ_{mix}, and not (directly) on M_{rp}.) We leave the effective temperature T_{rp} as a free parameter, deferring a more detailed discussion of our treatment of

emission from optically thin material (whether r-process-enriched or not) to Section 3.

With these simplifications, we can determine how the spectrum of a totally optically thin rCCSN differs from the r-process-free case, for a given ψ_{mix} and T_{rp}. For the range of T_{rp} we consider, which are broadly consistent with (admittedly limited) constraints from both theory (Hotokezaka et al. 2021) and observation (Kasliwal et al. 2022), the impacts of the r-process are most visible in the NIR. We therefore characterize the signal strength in terms of $\Delta(R - X)$, the change in $R - X$ color relative to the r-process-free SN case ($M_{rp} = 0$), where $X \in \{J, H, K\}$. All magnitudes are calculated using the AB system and generic Bessel filters.

Figure 2 shows how each color changes for $400\,\mathrm{K} \leqslant T_{rp} \leqslant 3000\,\mathrm{K}$ and $0 \leqslant \psi_{mix} \leqslant 0.95$. The signal strength increases with the mixing coordinate ψ_{mix} and for a given ψ_{mix} is maximal for T_{rp} with blackbody functions peaking at wavelengths within the NIR band under consideration. Regardless of T_{rp} and ψ_{mix}, the signal becomes easier to observe at longer wavelengths. However, for cases of low to moderate mixing ($\psi_{mix} \lesssim 0.3$) the color difference even in $R - K$ is $\lesssim 1.5$ mag for all T_{rp}.

While this difference may still seem substantial, it is important to bear in mind that models of nebular-phase emission are not well constrained in either the standard or r-process-enriched case. Relying exclusively on nebular observations may make it difficult to evaluate collapsars as r-process sites, particularly if the r-process matter is centrally concentrated (low ψ_{mix}). We therefore turn our attention to the pre-nebular (photospheric) phase.

2.2. Photospheric Phase

Observations in the photospheric phase (before the ejecta is fully transparent) can sidestep some of the complications inherent in the acquisition and analysis of nebular-phase data. First, r-process emission in the photospheric phase is better understood, thanks both to extensive theoretical studies of r-process elements' atomic structures, which enable descriptions of their behavior in local thermodynamic equilibrium (e.g., Kasen et al. 2013; Fontes et al. 2020; Tanaka et al. 2020), and to observations of kn170817 (Arcavi et al. 2017; Coulter et al. 2017; Drout et al. 2017; Evans et al. 2017; Kilpatrick et al. 2017; McCully et al. 2017; Nicholl et al. 2017; Shappee et al. 2017; Smartt et al. 2017; Soares-Santos et al. 2017; Kasliwal et al. 2022).

Second, the SN is brighter during the photospheric phase, and it is therefore easier to obtain high signal-to-noise ratio photometry across a range of wavelengths. Finally, early observations do not preclude late-time follow-up. To the contrary, they may be useful for filtering out the events most worthy of further attention during nebular epochs.

Despite these advantages, the photospheric phase presents its own set of challenges. While the ejecta remains optically thick, the r-process signal may be more difficult to discern than it would be during the nebular phase, due to overlapping, highly broadened spectral absorption features (e.g., Chornock et al. 2017; Kasen et al. 2017), and/or contamination from the r-process-free envelope. This is of particular concern early on, when the envelope is opaque and obscures emission from the enriched core underneath it. The position of the photosphere (the surface that divides optically thick from optically thin material) is therefore a good indicator of how observable an r-process signature is at a given time.

Table 1
Parameters of the *r*-process Collapsar Model

| Symbol	Definition
M_{ej}	The total mass of the ejecta
E_k	The kinetic energy of the ejecta
β_{ej}	The ejecta's average expansion velocity, normalized to c ($E_k = M_{ej}\beta_{ej}^2 c^2/2$)
M_{56}	The mass of radioactive ^{56}Ni produced in the explosion
M_{rp}	The mass of *r*-process material in the ejecta
M_{mix}	The mass of the ejecta enriched with *r*-process material ($\neq M_{rp}$)
ψ_{mix}	The fraction of M_{ej} that is enriched ($= M_{mix}/M_{ej}$)
ζ	The *r*-process mass fraction in the enriched layers ($= M_{rp}/M_{mix}$)
$\kappa_{sn} (=0.05~\mathrm{cm^2~g^{-1}})$	The gray opacity of SN ejecta containing no *r*-process material
$\kappa_{rp} (=10~\mathrm{cm^2~g^{-1}})$	The gray opacity of a pure *r*-process composition
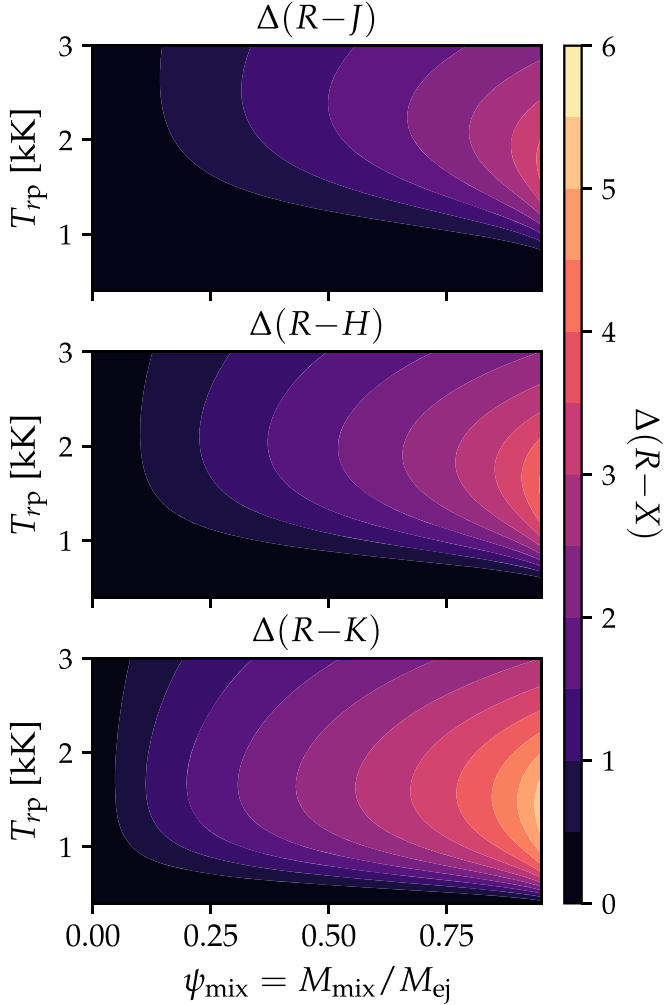
Figure 2. The addition of *r*-process material alters the optical−NIR colors of the nebular phase compared to SNe with no *r*-process enrichment. The magnitude of the effect depends on the mixing coordinate ψ_{mix} and on the nebular-phase *r*-process SED, which we model here as a blackbody of effective temperature T_{rp}. The signal is most apparent for high ψ_{mix} and for $1000~\mathrm{K} \lesssim T_{rp} \lesssim 2000~\mathrm{K}$.

To model the photospheric phase, we build on the simple ejecta structure introduced in Section 2.1. In addition to M_{ej}, we now describe the ejecta in terms of its kinetic energy E_k and explicitly consider the *r*-process mass fraction in the enriched layers, $\zeta = M_{rp}/M_{mix}$. This model directly corresponds to Figure 1 and makes use of the full set of parameters defined there and in Table 1.

As in Section 2.1, our analysis here rests on the distinct optical properties of *r*-process elements. We assume that the high opacity of the enriched regions causes them to shine in the NIR, significantly redder than both photospheric and nebular-phase emission from the *r*-process-free layers. (The assumption of an NIR-dominated SED is a good one for cores composed primarily of *r*-process elements; however, with increased mixing, both dilution and enhanced ionization due to energy from ^{56}Ni/Co decay may reduce the opacity, resulting in somewhat bluer emission; e.g., Barnes et al. 2021.)

While the effect of the high-opacity core will be subtle during the light curve's early stages, it will become more apparent as the photosphere, which forms at ever-lower mass coordinates, sinks into the *r*-process layers. At this point, the enriched core becomes "visible," and its higher opacity exerts a greater influence on the overall SED of the *r*CCSN.

This argument suggests that *r*-process enrichment will be easier to detect in explosions with larger ψ_{mix} and M_{rp}. Simple one-zone light-curve models allow us to map out this dependence. We focus here on times after the outer layers have become transparent. During this period, radiation from the photosphere originates entirely from *r*-process-enriched material, while optically thin emission comes predominantly from the *r*-process-free envelope. Both enriched and unenriched regions contain radioactive material, and both continue to radiate after becoming optically thin. However, the recession of the photosphere slows dramatically after it reaches the inner high-opacity *r*-process layers, ensuring that nebular emission from the envelope dominates nebular emission from the core ($L_{neb}^{sn} \gg L_{neb}^{rp}$) out to fairly late times. We therefore ignore for the time being the contribution of L_{neb}^{rp} and assume $L_{neb} = L_{neb}^{sn}$.

We define the ratio of the photospheric (*r*-process) and nebular (*r*-process-free) luminosities to be

$$\mathcal{R}_L \equiv L_{ph}^{rp}/L_{neb}^{sn}, \qquad (1)$$

and we adopt it as a rough indicator of the detectability of an *r*-process-enrichment signature.

We estimate (see Section 3 for more detail) that optically thin *r*-process-free material emits $\sim 55\%$ of its energy at NIR wavelengths ($1~\mu\mathrm{m} \leqslant \lambda \leqslant 2.5~\mu\mathrm{m}$). The strength of the NIR excess from the photosphere can then be approximated as $\approx L_{ph}^{rp}/0.55 L_{neb}^{sn}$. To produce an NIR signal $\sim 50\%$ stronger than expected from *r*-process-free nebular emission alone requires $\mathcal{R}_L \gtrsim 0.3$.

The *r*-process-detectability metric $\mathcal{R}_L$ depends on a few fundamental timescales. For a constant-density ejecta of mass M_{ej} and kinetic energy E_k, the *r*-process-free envelope becomes

transparent at

$$\tau_{\rm tr} = 53 \text{ days} \times \frac{M_{\rm ej}/M_\odot}{(E_k/1 \text{ foe})^{1/2}} \sqrt{1 - \psi_{\rm mix}^{1/3}},$$

$$\text{or} \left(\frac{\tau_{\rm tr}}{\tau_{\rm pk}}\right)^2 = 1.2 \frac{(1 - \psi_{\rm mix}^{1/3})}{\beta_{\rm ej}}, \quad (2)$$

where 1 foe $= 10^{51}$ erg and $\beta_{\rm ej}$ is the characteristic velocity in units of c ($E_{\rm k} = M_{\rm ej}\beta_{\rm ej}^2 c^2/2$). In the second line, we have normalized to the standard light-curve peak time, $\tau_{\rm pk} = 9$ days $(M_{\rm ej}/M_\odot)^{3/4}(E_{\rm k}/1 \text{ foe})^{-1/4}$, which, like the transparency time $\tau_{\rm tr}$, was calculated assuming an ejecta opacity of $\kappa_{\rm sn} = 0.05$ cm^2 g^{-1}, much lower than the opacity of r-process compositions. This choice presumes that the early light-curve evolution is driven by the unenriched layers, an assumption that becomes less reliable with increased outward mixing (higher $\psi_{\rm mix}$).

Once the unenriched layers are optically thin, their luminosity reflects the rate at which the material in those layers produces energy via radioactivity. Thus, for $t > \tau_{\rm tr}$, $L_{\rm neb}^{\rm sn}$ declines as ^{56}Ni/Co decay away. In contrast, emission from the r-process layers evolves on a distinct timescale set by their opacity and mass. It may be rising, maximal, or in decline at $\tau_{\rm tr}$. A second key timescale is therefore $\tau_{\rm rp}$, the time over which $L_{\rm ph}^{\rm rp}$ rises to a maximum. This can be estimated as the time to peak for a transient consisting solely of the inner enriched layers,

$$\tau_{\rm rp} = 9 \text{ days} \times \frac{(M_{\rm ej}/M_\odot)^{3/4}\psi_{\rm mix}^{1/3}}{(E_{\rm k}/1 \text{ foe})^{1/4}}[\zeta(\mathcal{K} - 1) + 1]^{1/2},$$

$$\text{or} \left(\frac{\tau_{\rm rp}}{\tau_{\rm tr}}\right)^2 = 0.9 \frac{\beta_{\rm ej}\psi_{\rm mix}^{2/3}}{(1 - \psi_{\rm mix}^{1/3})}[\zeta(\mathcal{K} - 1) + 1], \quad (3)$$

where $\zeta = M_{rp}/M_{\rm mix}$ is the r-process mass fraction of the enriched layers and $\mathcal{K} = \kappa_{rp}/\kappa_{\rm sn}$ is the ratio of the r-process opacity to the opacity of the (unenriched) SN ejecta. In normalizing to $\tau_{\rm tr}$, we have again assumed $\kappa_{\rm sn} = 0.05$ cm^2 g^{-1}. Since heavy r-process compositions have $\kappa_{rp} \approx 10$ cm^2 g^{-1} (Barnes & Kasen 2013; Tanaka & Hotokezaka 2013; Grossman et al. 2014), $\mathcal{K} \approx 200$.

If $\tau_{\rm tr}$ represents the *first* chance to observe emission from the r-process-enriched layers, $\tau_{\rm rp}$ is a proxy for the *best* chance—the point at which that emission component glows brightest. Thus, systems for which $\tau_{\rm rp} \approx \tau_{\rm tr}$ are close to ideal from an observability standpoint; the r-process layers are shining most strongly around the time they first come into view, when the SN overall is still fairly bright. If instead $\tau_{\rm rp} \ll \tau_{\rm tr}$, the luminosity from the inner r-process core begins its decline before it is even visible. (At the other extreme, for $\tau_{\rm rp} \gg \tau_{\rm tr}$, there is a danger that $L_{\rm ph}^{\rm rp}$ will climb to its peak only after the rCCSN overall has grown faint.) Thus, as we will see, the observability parameter $\mathcal{R}_{\rm L}$ is sensitive to $\tau_{\rm rp}/\tau_{\rm tr}$, and a successful observation is more likely when this ratio $\gtrsim 1$.

The value of $\tau_{\rm rp}/\tau_{\rm tr}$ depends on the interplay between $\psi_{\rm mix}$, ζ, and $\beta_{\rm ej}$, as expressed in Equation (3). Not surprisingly, for constant $\beta_{\rm ej}$, $\tau_{\rm rp}/\tau_{\rm tr}$ increases with both the mixing coordinate ($\psi_{\rm mix}$) and the r-process mass fraction in the core (ζ). However, if $\beta_{\rm ej}$ is sufficiently high, $\tau_{\rm rp}/\tau_{\rm tr}$ can approach unity even for low $\psi_{\rm mix}$ and ζ. This can be seen in Figure 3, which plots the contours at which $\tau_{\rm rp}/\tau_{\rm tr} = 1$ for different $\beta_{\rm ej}$. As Figure 3 illustrates, higher-velocity outflows will offer opportunities to
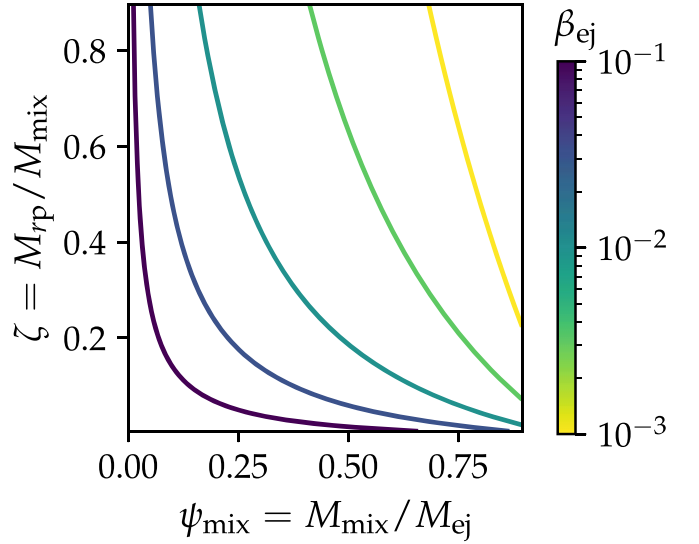

Figure 3. R-process signals will be easier to see if the peak time of the enriched inner layers (τ_{rp}) is close to the time at which the outer layers become transparent ($\tau_{\rm tr}$). This is the case only for certain combinations of the mixing coordinate $\psi_{\rm mix}$ ($=M_{\rm mix}/M_{\rm ej}$), the r-process mass fraction ζ ($=M_{rp}/M_{\rm mix}$), and the velocity $\beta_{\rm ej}$. The curves above denote the contours where $\tau_{rp} = \tau_{\rm tr}$ for different values of $\beta_{\rm ej}$. For higher $\beta_{\rm ej}$, $\tau_{rp} \approx \tau_{\rm tr}$ even for low $\psi_{\rm mix}$ and/or low ζ. In contrast, for lower $\beta_{\rm ej}$, the signal is weaker absent significant mixing.

observe r-process enrichment for a greater variety of enrichment parameters ($\psi_{\rm mix}$ and ζ).

However, even if the timescales are favorable ($\tau_{\rm rp} \approx \tau_{\rm tr}$), the r-process-visibility parameter $\mathcal{R}_{\rm L}$ is limited by $\psi_{\rm mix}$; only energy deposited behind the photosphere can be emitted from behind the photosphere. Our models have uniformly distributed ^{56}Ni, which establishes $\psi_{\rm mix}/(\psi_{\rm mix} - 1)$ as a fundamental scale for $\mathcal{R}_{\rm L}$. According to Arnett's law (Arnett 1980, 1982), $\mathcal{R}_{\rm L}$ reaches a maximum of $\psi_{\rm mix}/(1 - \psi_{\rm mix})$ at $t = \tau_{\rm rp}$.

We estimate $L_{\rm ph}^{\rm rp}$ at $t \sim \tau_{\rm rp}$ by Taylor-expanding the analytic light-curve solution to a one-zone model of a radioactively powered transient (Chatzopoulos et al. 2012),[4]

$$L_{\rm ph}^{\rm rp}(t \sim \tau_{rp}) \approx \psi_{\rm mix} M_{56}\left[\dot{\epsilon}_{56}(\tau_{rp}) - \frac{1}{2}\frac{(t - \tau_{rp})^2}{\tau_{rp}\tau_{\rm Ni}}\right.$$

$$\left. \times (\dot{\epsilon}_{56}(\tau_{rp}) - \dot{\epsilon}_{\rm Co,eq}(\tau_{rp}))\right], \quad (4)$$

where

$$\dot{\epsilon}_{\rm Co,eq}(t) = \frac{q_{\rm Co}}{\tau_{\rm Co}} \exp\left[\frac{-t}{\tau_{\rm Co}}\right].$$

In Equation (4), M_{56} is the ^{56}Ni mass, $\dot{\epsilon}_{56}$ is the rate of specific energy production by ^{56}Ni and ^{56}Co decay, and $\tau_{\rm Ni}$ ($\tau_{\rm Co}$) is the ^{56}Ni (^{56}Co) lifetime. The quantity $q_{\rm Co}$ is the decay energy of

---

[4] The equation of energy conservation in a homologously expanding, diffusive, homogeneous medium heated by radioactive decay gives an expression for the time-dependent emerging luminosity,

$$L(t) = \exp\left(\frac{-t^2}{2\tau_{\rm lc}^2}\right)\left[\int_0^t \dot{Q}_{\rm rad}(t')\left(\frac{t'}{\tau_{\rm lc}^2}\right)\exp\left(\frac{t'}{2\tau_{\rm lc}^2}\right)dt'\right],$$

where $\tau_{\rm lc}$ is a characteristic light-curve timescale defined in the same way as $\tau_{\rm pk}$ and $\tau_{\rm rp}$. Expanding this solution about $t = \tau_{\rm lc}$, with the specification that the radioactive heating $\dot{Q}_{\rm rad}$ is due solely to ^{56}Ni/Co decay (reasonable for $M_{rp} \lesssim M_{56}$, especially at early times), yields Equation (4).
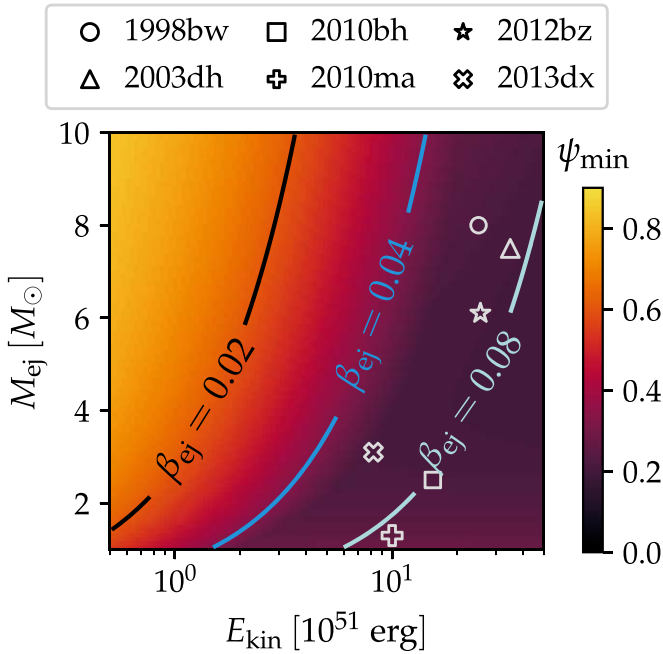
Figure 4. *R*-process signatures may be detectable in the photospheric phase if ejecta velocities are high—even for low mixing coordinates $\psi_{\rm mix}$. Colored regions indicate the minimum mixing coordinate ($\psi_{\rm min}$) for which $M_{rp} = 0.05$ $M_\odot$ produces a detectable signal, as a function of $M_{\rm ej}$ and $E_{\rm k}$. Lines of constant $\beta_{\rm ej}$ are overplotted. As described in the text, to be observable, a signal must fulfill both (a) $\tau_{\rm tr} \leqslant 3\tau_{\rm pk}$ and (b) $\mathcal{R}_{\rm L} \geqslant 0.3$ at any time $\tau_{\rm tr} \leqslant t \leqslant 3\tau_{\rm pk}$. A deeply buried *r*-process core (small $\psi_{\rm mix}$) is difficult to observe except in cases of low $M_{\rm ej}$ and/or high $E_{\rm k}$. For typical SN Ib/c parameters ($M_{\rm ej}/M_\odot \sim$ a few, $\beta_{\rm ej} \sim 0.03$), *r*-process detection will be challenging unless mixing is extensive. On the other hand, the higher velocities of SNe Ic-BL, including GRB-SNe, should facilitate detection, even for low $\psi_{\rm mix}$. Scatter markers show $E_{\rm k}$ and $M_{\rm ej}$ for a handful of observed SNe (with error bars omitted to improve readability) from Cano et al. (2017).

^{56}Co divided by its mass. Since we approximate the nebular luminosity from the *r*-process free layers as

$$L_{\rm neb}^{\rm sn} = (1 - \psi_{\rm mix})M_{56}\dot{\epsilon}_{56},$$

Equation (4) enables a straightforward determination of $\mathcal{R}_{\rm L}$, once all model parameters have been specified.

This framework allows us to estimate, given $M_{\rm ej}$ and $E_{\rm k}$, the minimum $\psi_{\rm mix}$ for which some *r*-process mass M_{rp} can produce an "observable" signal—i.e., one that produces a strong NIR excess on a timescale not too delayed relative to the light-curve peak. This estimate is shown in Figure 4 for $M_{rp} = 0.05$ $M_\odot$, an *r*-process mass comparable to what was produced in GW170817 (Abbott et al. 2017a; Kasen et al. 2017; Kasliwal et al. 2017; Tanaka et al. 2017). In calculating $\psi_{\rm min}$, we defined an observable signal as one for which (a) $\tau_{\rm tr} \leqslant 3\tau_{\rm pk}$ and (b) $\mathcal{R}_{\rm L}$ reaches a maximum $\geqslant 0.3$ at some point in the interval $\tau_{\rm tr} \leqslant t \leqslant 3\tau_{\rm pk}$. The first criterion addresses whether the *r*-process signal will appear before the light curve has dimmed significantly, while the second requires the signal to be strong enough to appreciably alter the SED from the optically thin *r*-process-free ejecta.

Applying these conditions, we find (for $M_{rp} = 0.05$ $M_\odot$) that SNe with low mixing coordinates ($\psi_{\rm mix} \lesssim 0.4$) generate a visible *r*-process signal only for $\beta_{\rm ej} \gtrsim 0.04c$. This is somewhat larger than typical SN Ib/c velocities, but not uncommon for higher-energy GRB-SNe, whose velocities cluster in the range $\beta_{\rm ej} = 0.057 \pm 0.013$ (Modjaz et al. 2016). To better illustrate this point, we have plotted in Figure 4 the inferred $E_{\rm k}$ and $M_{\rm ej}$

for several observed GRB-SNe, which we take from Cano et al. (2017). Fortuitously, our analysis suggests that the high-velocity SNe Ic-BL connected to long GRBs— i.e., the SNe most likely to be associated with collapsars, and hence significant *r*-production—are the same events for which *r*-process enrichment is detectable even for low $\psi_{\rm mix}$.

Despite the simplifications invoked in the preceding analysis, these trends suggest that rCCSN search strategies need not be limited to the nebular phase. Indeed, they motivate a more rigorous consideration of the full evolution of *r*CCSN light curves.

3. Semianalytic Light-curve Modeling

We use a semianalytic framework to model the emission from *r*-process-enriched and unenriched SNe from the initial explosion through to the nebular phase.

3.1. Basic Structure

We begin with ejecta composed of concentric, homologously expanding spherical shells. The density and composition of each shell are parameters of the model, and the frequency-independent (gray) opacity is a function of the local temperature and composition.

The internal energy of a shell *i* evolves as

$$\frac{dE_{\text{int},i}}{dt} = \dot{Q}_{\text{rad},i} - \frac{E_{\text{int},i}}{t} - L_i, \quad (5)$$

where $\dot{Q}_{\text{rad},i}$ is the power injected by radioactive decays (in this case, of ^{56}Ni, ^{56}Co, and *r*-process nuclei), and $E_{\text{int},i}/t$ accounts for adiabatic losses. The radiated luminosity L_i depends on the local diffusion ($t_{\rm diff}$) and light-crossing ($t_{\rm cross}$) timescales,

$$L_i = \frac{E_{\text{int},i}}{t_{\text{diff},i} + t_{\text{cross},i}},$$

with

$$t_{\text{diff},i} = \frac{2}{c}\sum_{j \geqslant i} \rho_j \kappa_j r_j \Delta r_j$$

and

$$t_{\text{cross},i} = \frac{r_i}{c},$$

where ρ_i is the mass density of shell *i*, κ_i its opacity, r_i its current radius, and Δr_i its radial width. The emerging bolometric luminosity at any time *t* is a sum over L_i,

$$L_{\rm bol}(t) = \sum_i L_i.$$

In an optically thick system, radiation tends toward a blackbody distribution. For a gray-opacity medium like ours, the photosphere is well defined and the relationship between the luminosity and the SED is straightforward,

$$L(t) = 4\pi r_{\rm ph}^2 \sigma_{\rm SB} T_{\rm eff}^4$$

and

$$L_\nu = 4\pi^2 r_{\rm ph}^2 B_\nu(T_{\rm eff}), \quad (6)$$

where $\sigma_{\rm SB}$ is the Stefan–Boltzmann constant, $r_{\rm ph}$ is the radius of the photosphere, $T_{\rm eff}$ is the effective temperature, and B_ν is the Planck function.

As the ejecta becomes increasingly transparent, the blackbody approximation becomes less and less reliable. We are interested in modeling the emission of the SN as it transitions from optically thick to optically thin, which motivates a modification of the blackbody prescription of Equation (6). As in Section 2, we categorize the emerging luminosity as *photospheric* if it originates interior to the radius $r_{\rm ph}$ defined by $\tau = \int_{r_{\rm ph}}^{\infty} \rho(r') \kappa(r') dr' = 2/3$, and *nebular* otherwise.

The photospheric component, $L_{\rm ph}$, is translated to an SED via Equation (6). The rigorous numerical modeling required to predict the emission of the nebular component is beyond the scope of this work. Instead, we assume that the SED of radiation from optically thin regions depends only on the composition of the zone where it originates. Building on the discussions in Sections 2.1 and 2.2, we associate one characteristic nebular SED with *r*-process-free SN ejecta and a second one with the *r*-process. The net SED from an optically thin zone is a scaled sum of the two, as explained in Section 3.2.

3.2. Implementation of the Model

We apply this blueprint to regular and *r*CCSN models characterized by the same parameters as in Section 2: ejecta mass ($M_{\rm ej}$) and velocity ($\beta_{\rm ej}$), ^{56}Ni mass (M_{56}), the *r*-process mass M_{rp} (equal to zero for unenriched SNe), and, for $M_{rp} > 0$, the mixing coordinate $\psi_{\rm mix}$. All models have a uniform distribution of ^{56}Ni and a broken power-law mass density profile, $\rho \propto (v/v_{\rm tr})^{-\alpha}$, where $\alpha = 1$ (10) for $v < (\geqslant) v_{\rm tr}$, and the transition velocity $v_{\rm tr}$ is chosen to ensure that $\rho(v)$ integrates to the desired $M_{\rm ej}$ and $E_{\rm k} (= M_{\rm ej} \beta_{\rm ej}^2 c^2/2)$.

The decays of ^{56}Ni/Co and, if present, *r*-process nuclei supply the energy ultimately radiated by the SN. We assume that γ-rays from ^{56}Ni and ^{56}Co, which constitute most of the energy from that decay chain, are deposited in the zone that produced them with an efficiency $f_{\rm dep,\gamma}$ that depends on τ_γ, the ejecta's global optical depth to γ-rays. We adopt the functional form of Colgate et al. (1980) for $f_{\rm dep,\gamma}(\tau_\gamma)$ and calculate τ_γ using their suggested γ-ray opacity $\kappa_\gamma = 1.0/35.5$ cm^2 g^{-1}. The fast positrons from the β^+-decay of ^{56}Co are assumed to thermalize locally and instantaneously.

For the M_{rp} and M_{56} we consider, the energy from *r*-process decay is subdominant to that from ^{56}Ni on the timescales of interest (SBM19). Thus, while we include energy from *r*-process radioactivity in $\dot{Q}_{\rm rad,\, i}$ (Equation (5)), we forgo complex treatments of the decay phase (e.g., Barnes et al. 2021) in favor of a power-law model (Metzger et al. 2010; Korobkin et al. 2012),

$$\dot{\epsilon}_{\rm rp} = 3 \times 10^{10} \left(\frac{t}{1 \text{ day}}\right)^{-1.3} \text{ erg s}^{-1} \text{ g}^{-1}.$$

We assume that 40% of this energy is in γ-rays, which thermalize in the same way as γ-rays from ^{56}Ni and ^{56}Co. We divide the remaining energy between β-particles (35%), which thermalize with perfect efficiency, and neutrinos, which do not thermalize at all. This simplified treatment is justified by the subdominance of $\dot{\epsilon}_{\rm rp}$, and by the high densities in the enriched regions compared to the densities expected in kilonovae (Bauswein et al. 2013; Hotokezaka et al. 2013; Kyutoku et al. 2015; Bovard et al. 2017; Radice et al. 2018), which supports efficient thermalization (Barnes et al. 2016).

We model only emission derived from radioactivity. In the case of a GRB-SN, the GRB afterglow could contribute to, or even dominate, optical and NIR emission at some epochs. However, as we will show, the timescales of interest for *r*-process detection are generally much longer than the timescales on which the afterglow fades away, and contamination is not a major concern.

Opacity in our model is wavelength independent but varies with temperature and composition. Ejecta free of both ^{56}Ni and *r*-process elements is assigned a baseline opacity $\kappa_{\rm sn} = 0.05$ cm^2 g^{-1}, consistent with Section 2.2. The effects on opacity of ^{56}Ni and its daughter products are accounted for with a simplified scheme, in which

$$\kappa_{56}(T) = \begin{cases} \kappa_{56,0} & \text{for } T < T_\kappa \\ \kappa_{56,0} \left(\dfrac{T}{T_\kappa}\right)^{4/3} & \text{for } T_\kappa \leqslant T \leqslant 2.5 \times 10^4 \text{ K} \\ 0.1 \text{ cm}^2\text{g}^{-1} & \text{for } T > 2 \times 10^4 \text{ K}, \end{cases}$$

where $T_\kappa = 3500$ K and the lower limit $\kappa_{56,0} = 0.01$ cm^2 g^{-1} reflects the dominance of electron-scattering opacity at low temperatures with a limited number of bound-bound transitions. This approximation is based on Planck mean opacities calculated for a mixture of ^{56}Ni, ^{56}Co, and ^{56}Fe (e.g., Kasen et al. 2013).

The total opacity in a zone is then given by

$$\kappa_i = \kappa_{\rm sn}(1 - X_{rp,i} - X_{56}) + \kappa_{rp} X_{rp,i} + \kappa_{56}(T_i) X_{56}, \quad (7)$$

where $\kappa_{rp} = 10$ cm^2 g^{-1} is the opacity of a pure *r*-process composition (Kasen et al. 2013; Tanaka & Hotokezaka 2013; Grossman et al. 2014), the *r*-process mass fraction $X_{rp,i}$ is ζ within the enriched core and zero elsewhere, and the ^{56}Ni mass fraction X_{56} equals $M_{56}/M_{\rm ej}$ in all zones. The zone's temperature T_i is a function of its internal energy density.

Equation (7) allows the determination of the photosphere and the demarcation of the optically thin region. As alluded to in Section 3.1, emission from optically thin zones is modeled as the linear combination of two distinct SEDs associated with *r*-process and *r*-process-free material (see Figure 1). The SEDs are empirically derived and independent of time and therefore elide the complex physics of nebular-phase spectral formation and evolution (e.g., Jerkstrand 2017). Nevertheless, *r*-process modeling (Hotokezaka et al. 2021) and SN observations (Gómez & López 2002; Tomita et al. 2006; Taubenberger et al. 2009) suggest that emission in the nebular phase may be fairly uniform in time and across different events, at least at the level of photometry. Furthermore, we find that this approach reproduces the photometry of SNe Ic with reasonable fidelity.

As mentioned in Section 2, we construct the *r*-process-free SED from the late-time *B*- through *K*-band photometry of SN 2007gr (Hunter et al. 2009; Bianco et al. 2014), accessed via the Open Supernova Catalog[5] (OSC; Guillochon et al. 2017). We consider data from $t \approx 120$ days after *B*-band maximum and perform a spline fit to convert photometry-derived monochromatic luminosities to a continuous SED, $\mathcal{F}_\nu^{07\text{gr}}$, as shown in Figure 5. To improve the agreement between our model and SN Ic/Ic-BL observations, we assume that 30% of the energy in this SED falls blueward of *U* or redward of *K*.
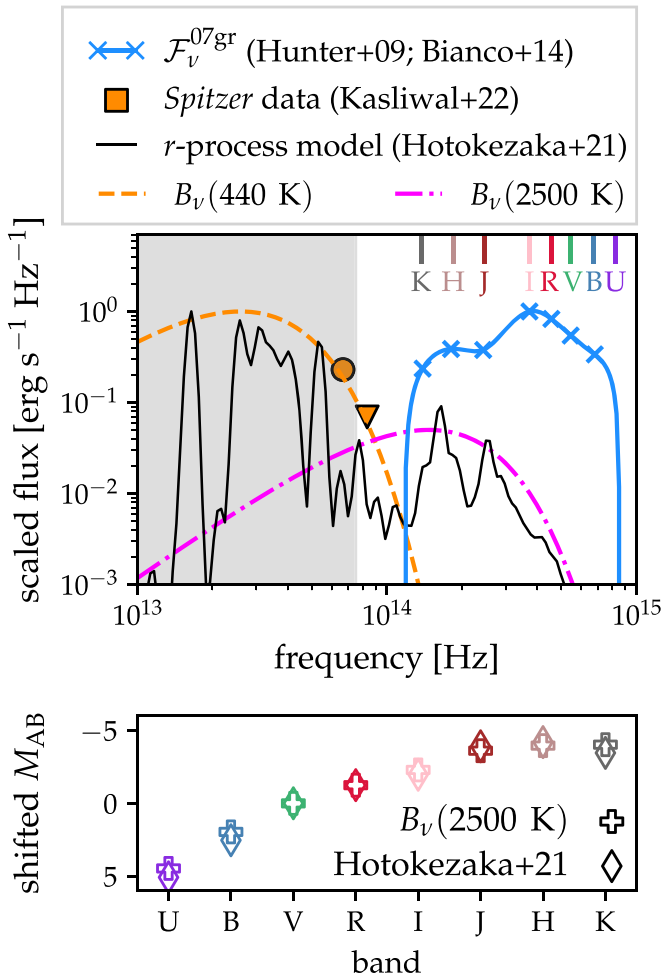
---

[5] R.I.P.

Figure 5. Top panel: our optically thin emission models and the observations and/or calculations that inform them. Optically thin layers free of r-process material emit a spectrum $\mathcal{F}_\nu^{07\mathrm{gr}}$ (blue curve) constructed from the photometry of the SN Ic SN 2007gr (Hunter et al. 2009; Bianco et al. 2014) 120 days after B-band maximum. The photometry-derived fluxes used in the spline fit are plotted as blue crosses. Observations of kn170817 43 days after the merger (Kasliwal et al. 2022; orange markers) are consistent with a blackbody at $T \lesssim 440$ K (dashed orange curve) or with the more complex spectrum (solid black line) predicted by Hotokezaka et al. (2021) for r-process compositions in the nebular phase. We adopt a scaled 2500 K blackbody SED (dotted-dashed pink curve) to approximate optically thin emission associated with r-process material. The frequencies of the UVOIR and NIR bands are shown on the top axis. The shaded region indicates the frequencies that will be accessible to the JWST. Bottom panel: AB magnitudes calculated from a blackbody at $T = 2500$ K (plus signs) and from the spectrum of (Hotokezaka et al. 2021; diamonds), both scaled so $M_V = 0$. The simpler blackbody function nevertheless faithfully reproduces the colors of the more complex spectrum.

The SED associated with optically thin r-process compositions is highly uncertain. Spitzer observations (Villar et al. 2018; Kasliwal et al. 2022) of kn170817 (the only definitive r-process transient detected to date) at 43 days post-explosion yielded one mid-infrared (MIR) photometric point and one upper limit. As Kasliwal et al. (2022) pointed out, if the kilonova's spectrum is a blackbody, these measurements constrain its temperature to $\lesssim 440$ K.

On the other hand, nebular-phase spectra are not expected to conform to a Planck function. Indeed, numerical modeling by Hotokezaka et al. (2021) of the emission from a nebula with properties similar to a collapsar disk wind and composed purely of neodymium (a high-opacity element synthesized by the r-process) predicted a spectrum with far more complexity than a

blackbody. While their results showed MIR emission consistent with the observations of Kasliwal et al. (2022), they also found significant flux at lower wavelengths. However, while nebular-phase *spectra* are unlikely to resemble a Plank function, we found that a blackbody at $T_{\mathrm{rp}} = 2500$ K nonetheless reproduces the *photometric colors* predicted by the optical and NIR regions of the spectrum of Hotokezaka et al. (2021). (The MIR component accounts for $\sim 60\%$ of the total energy but is too red to impact the photometry; it can be incorporated into the model SED simply by scaling the Plank function.) Figure 5 shows both the observations and the numerical model, as well as blackbody spectra for select temperatures, which we present for comparison. In the bottom panel, we show broadband magnitudes calculated for the Hotokezaka et al. (2021) spectrum and for our blackbody approximation to it, which agree well despite our simplifications.

The calculation of Hotokezaka et al. (2021) relies on a simplified model of pure r-process ejecta; neither the assumed composition nor the heating rate (due exclusively to r-process decay) maps directly onto the collapsar context. However, the argument for a bimodal spectrum is supported by simple arguments about r-process elements' atomic structures, which may be robust against increasing model complexity due to the distribution in energy space of permitted and dipole-forbidden atomic transitions (Hotokezaka et al. 2021). In the absence of additional data, we therefore approximate the r-process-associated SED as a blackbody at 2500 K, which we scale to account for the out-of-band emission. Though some of our zones are r-process-free, none are purely r-process; at a minimum, each zone contains a mixture of r-process elements and ^{56}Ni. The appropriate way to model nebular emission from zones with complex compositions is an additional uncertainty. Nebular spectra are dominated by the species that cool most efficiently, which may be distinct from the most abundant elements.

Here, we move away from the simpler approach of Section 2.1 and allocate the luminosity of an optically thin zone according to the fraction of the total optical depth a given component provides across that zone. For r-process material, that fraction is

$$f_{\mathrm{rp},i} = \frac{\kappa_{\mathrm{rp}} X_{\mathrm{rp},i}}{\kappa_i},$$

with κ_i defined by Equation (7). Thus, the luminosity $L_{\mathrm{neb},i}$ from a zone outside the photosphere is converted to an SED following

$$L_{\mathrm{neb},i,\nu} = L_{\mathrm{neb},i,\nu}^{\mathrm{rp}} + L_{\mathrm{neb},i,\nu}^{\mathrm{sn}},$$

where

$$L_{\mathrm{neb},i,\nu}^{\mathrm{rp}} = 0.41 \times f_{\mathrm{rp},i}\, \frac{\pi L_{\mathrm{neb},i}}{\sigma_{\mathrm{SB}} T_{\mathrm{rp}}^4}\, B_\nu(T_{\mathrm{rp}}),$$
$$T_{\mathrm{rp}} = 2500 \text{ K},$$

and

$$L_{\mathrm{neb},i,\nu}^{\mathrm{sn}} = 0.7 \times (1 - f_{\mathrm{rp},i})\, L_{\mathrm{neb},i}\, \mathcal{F}_\nu^{07\mathrm{gr}}.$$

3.3. Model Validation

We validated our semianalytic model against a handful of SNe Ic/Ic-BL with late-time multiband photometry. In Figure 6, we show our predictions alongside observations for
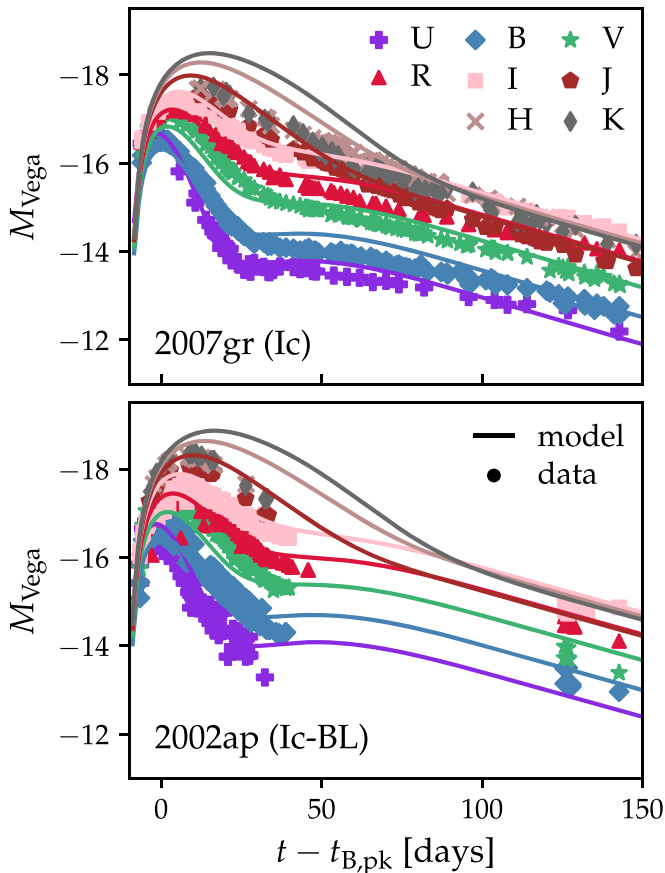
Figure 6. A comparison of model photometry (solid lines) and observations (markers) shows that our approach is well suited for modeling SNe Ic at a range of kinetic energies. SN 2007gr (top panel) is classified as an ordinary SN Ic (Madison & Li 2007), while SN 2002ap (bottom panel) is an SN Ic-BL (Filippenko & Chornock 2002; Gal-Yam et al. 2002; Meikle et al. 2002). The model parameters for each SN are given in Table 2. Photometry is from Bianco et al. (2014), courtesy of the OSC (Guillochon et al. 2017), and from Yoshii et al. (2003) and references therein. To improve readability, in these plots only we calculate magnitudes using the Vega system.

Table 2
Model Parameters Adopted in Figure 6

SN	$M_{\rm ej}/M_\odot$	$E_{\rm k}/10^{51}$ erg	$M_{56}/M_\odot$
2007gr[a]	2.0 (2.0–3.5)	3.2 (1.0–4.0)	0.08 ($0.076^{+0.02}_{-0.02}$)
2002ap[b]	3.2 (2.5–5.0)	4.4 (4.0–10.0)	0.11 (0.07)

Notes.
[a] Inferred ejecta properties for SN 2007gr (in parentheses) from Hunter et al. (2009).
[b] Inferred ejecta properties for SN 2002ap (in parentheses) from Deng et al. (2003).

Table 3
Parameters of the Model Suite

Quantity	Minimum	Maximum	N[a]	Spacing
$M_{\rm ej}$	$0.5\,M_\odot$	$12\,M_\odot$	24	logarithmic
$\beta_{\rm ej}$	0.01	0.25	25	logarithmic
M_{56}	$0.05\,M_\odot$	$1.0\,M_\odot$	20	logarithmic
$\psi_{\rm mix}$	0.1[b]	0.9	$\leqslant 10$	linear
M_{rp}	$(0.0\,M_\odot)$, $0.01\,M_\odot$, $0.03\,M_\odot$, $0.08\,M_\odot$, $0.15\,M_\odot$			

Notes.
[a] The number of distinct values considered for each quantity.
[b] For every choice of $M_{\rm ej}$, M_{56}, and M_{rp} there is a minimum $\psi_{\rm mix}$ for which the enriched core contains only ^{56}Ni and r-process elements. Values of $\psi_{\rm mix}$ for each model include this minimum, ψ_0, and all $\psi_{\rm mix}$ indicated above for which $\psi_{\rm mix} > \psi_0$.

one ordinary and one broad-lined SN Ic. The model parameters we used, as well as inferred ejecta properties reported in the literature, are recorded in Table 2. Despite its simplifications, our model reproduces the basic features of the SNe, suggesting that we are accounting for the most important physical processes driving the light curve's evolution.

Around maximum light, our model is most accurate in ultraviolet and optical bands. Though a lack of data makes it harder to gauge model performance in the NIR, the data that are available suggest that we may overpredict J, H, and K magnitudes in the light curve's early phases. However, we focus on optical−NIR color *difference* as an r-process signature (e.g., Section 2.1, Section 4). Thus, slightly overestimating the NIR emission of r-process-free SNe near peak will merely make our calculation more conservative. Enriched models that are redder (in $R - J$, $R - H$, and/or $R - K$) than our unenriched models would be *much* redder than true SNe, meaning that the color differences we predict are likely to be underestimates, and the actual r-process signal may be stronger than we forecast.

We also found that our model is slightly less successful at reproducing the photometry of SNe Ic-BL. This is perhaps not surprising considering that the extreme kinetic energies ($\sim 10^{52}$ erg) of SNe Ic-BL, as well as the GRBs sometimes observed in conjunction with them, point to a nonstandard

(e.g., "engine-driven") explosion mechanism that may induce ejecta asymmetries or unusual density profiles (e.g., Maeda et al. 2003; Tanaka et al. 2008; Barnes et al. 2018). They are also the SNe most closely linked, theoretically, to the collapsar explosion model (e.g., Woosley & Bloom 2006), and therefore the most likely to produce emission-altering r-process elements. Having validated our approach, we next use it to model the emission from enriched and unenriched SNe across a broad parameter space.

3.4. Construction of A Model Suite

We construct multiband light curves extending to $t = 200$ days after explosion for r-process-enriched and unenriched SNe with a range of explosion and r-process-enrichment properties. The parameter values used in the model suite are presented in Table 3. We require that radioactive material not dominate the total ejecta mass (i.e., we enforce $M_{56} \leqslant 0.5 M_{\rm ej}$ and $M_{rp} \leqslant 0.5(M_{\rm ej} - M_{56})$), and we do not consider models with kinetic energies $E_{\rm k} > 5 \times 10^{52}$ erg. Beyond these constraints, all parameter combinations are explored, even those that produce SNe with kinetic energies somewhat lower than would be expected for a collapsar origin. The r-process-free models reproduce the range of luminosities and timescales of observed SNe Ic and SNe Ic-BL (Drout et al. 2011; Perley et al. 2020), which validates both our modeling framework and the range of parameter values we adopt.

We do not consider here the case of complete mixing ($\psi_{\rm mix} = 1$). For fully mixed models, the high opacity of the r-process elements would affect the SN emission from the explosion onward, resulting in a transient very distinct from ordinary SNe at all phases of its evolution. The question of detecting fully mixed rCCSNe (or of recognizing one should it turn up in a blind search) is therefore better deferred to a
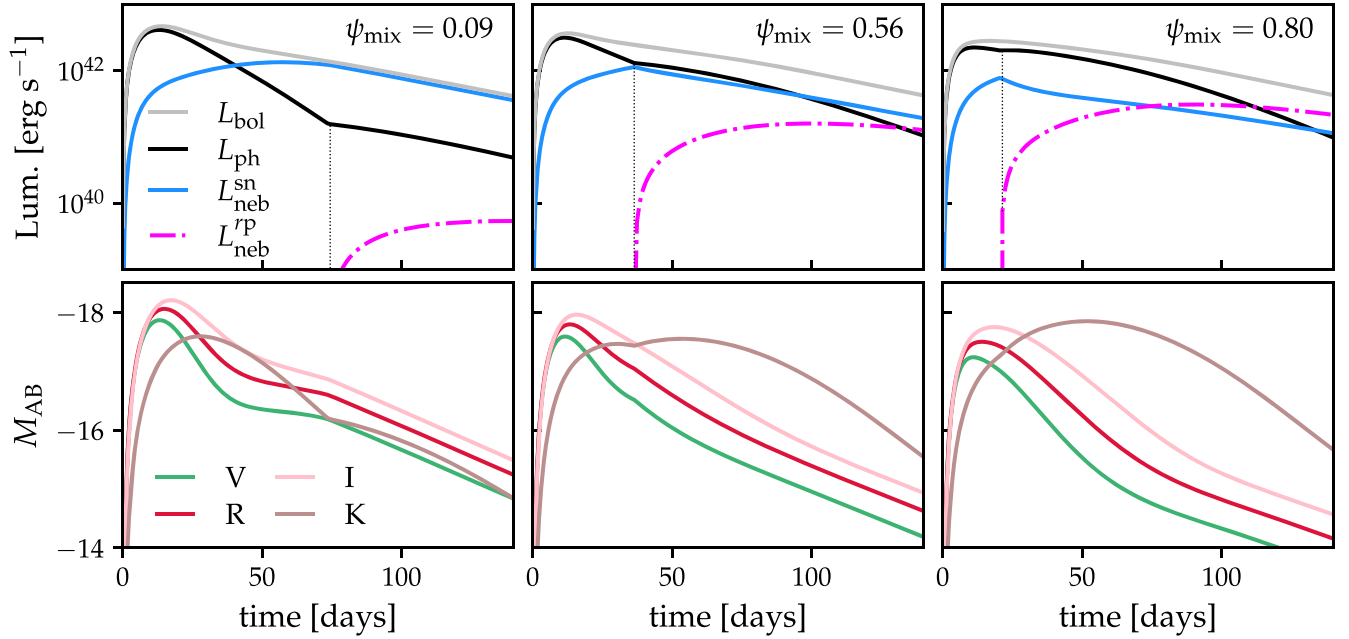
Figure 7. Increased mixing enhances emission in the NIR relative to the optical. All models above have $M_{\rm ej} = 4.0\ M_\odot$, $\beta_{\rm ej} = 0.04$, $M_{56} = 0.25\ M_\odot$, and $M_{rp} = 0.08\ M_\odot$. Top panels: mixing redistributes energy among luminosity components, with higher $\psi_{\rm mix}$ favoring $L_{\rm ph}$ and $L_{\rm neb}^{rp}$ over $L_{\rm neb}^{\rm sn}$. (Note that $L_{\rm neb}^{\rm sn}$ and $L_{\rm neb}^{rp}$ refer to luminosity components with distinct SEDs, rather than components emitted from r-process-rich or -free regions. As described in Section 3.2, enriched ejecta contributes energy to both $L_{\rm neb}^{\rm sn}$ and $L_{\rm neb}^{rp}$.) The dotted black lines indicate $t = \tau_{\rm tr}$, the time at which the outer r-process-free layers become transparent. The evolution of $L_{\rm ph}$ slows at this point in response to the higher opacity of the core. Bottom panels: select broadband light curves showing the redistribution of energy from bluer to redder wavelengths.

separate work (though it has been at least partially addressed by Siegel et al. 2021, who discuss electromagnetic counterparts from very massive, uniformly mixed, r-process-enhanced "superkilonovae"). We focus instead on rCCSNe with at least a small outer shell of r-process-free material. This conceals the effects of the r-process initially, allowing such rCCSNe to masquerade (if only for a limited time) as unenriched SNe.

4. Results

We first explain how the addition of r-process material influences the evolution of SNe with specified explosion parameters ($M_{\rm ej}$, $\beta_{\rm ej}$, and M_{56}). We then adopt a wider lens and consider how signs of r-process enrichment may manifest in SNe with different observational properties. Finally, we consider how our analysis could inform rCCSN search strategies.

4.1. Effects of r-process Enrichment on SN Emission

Enriching SN ejecta with r-process elements extends the photospheric phase and alters the SED from the optically thin layers. Each of these effects shifts the emitted spectrum from the optical toward the NIR; however, the strength of this shift and the timescale at which it occurs depend on the mass of r-process material (M_{rp}) and how extensively it is mixed in the ejecta ($\psi_{\rm mix}$).

The response of bolometric and broadband light curves to $\psi_{\rm mix}$ is illustrated in Figure 7. When the r-process is concentrated in the ejecta's center, its influence is minimal, since only a negligible fraction of the radiation originates in the enriched layers. At higher $\psi_{\rm mix}$, the effects are more visible. The extended high-opacity core limits diffusion from the interior, producing lower $L_{\rm bol}$ and $L_{\rm ph}$ near peak. After the outer layers reach transparency, the opaque core slows—or even reverses—the recession of the photosphere, sustaining a higher

$L_{\rm ph}$ at the expense of $L_{\rm neb}^{\rm sn}$. As the enriched layers (slowly) become transparent, their nebular emission begins to contribute to $L_{\rm neb}^{rp}$, and for high enough $\psi_{\rm mix}$ or late enough epochs, $L_{\rm neb}^{rp}$ can overpower $L_{\rm neb}^{\rm sn}$.

The long-lived photosphere and the r-process nebular component each provide a luminous source of low-temperature emission that impacts the evolution of the SED and, therefore, the broadband light curves. The net effect is a transfer of energy from optical to NIR bands, as can be seen in the bottom panels of Figure 7. The greater the mixing, the more dramatic the redistribution.

As seen in Figure 7, mixing also affects light-curve shapes, though not always in a straightforward way. In most cases, the opacity of the core is high enough that emission from the r-process-rich and r-process-free layers effectively becomes decoupled, rising to distinct peaks on distinct timescales (e.g., Section 2.2). Unless $\psi_{\rm mix}$ is very high, diffusion from the core is suppressed to the degree that the peak of $L_{\rm ph}$ is driven mainly by the r-process-free ejecta. Increasing $\psi_{\rm mix}$ reduces the mass and increases the average velocity of this ejecta component, producing a narrower peak in $L_{\rm ph}$ and sharper light curves in optical bands, despite the increasing spatial extent of the high-opacity region.

To better understand how r-process-enriched SNe may be distinguished from their r-process-free counterparts, we expand the parameter space of Figure 7, enriching a single explosion model ($M_{\rm ej}$, $\beta_{\rm ej}$, M_{56}) = (4.0 $M_\odot$, 0.04, 0.25 $M_\odot$) with a range of M_{rp} at various $\psi_{\rm mix}$. We calculate the broadband evolution for each combination (M_{rp}, $\psi_{\rm mix}$) and compare the colors to those of an r-process-free SN with the same $M_{\rm ej}$, $\beta_{\rm ej}$, and M_{56}.

Because the effects of enrichment are seen primarily in the NIR, we use $R - X$ color as a proxy for the r-process signal strength, with $X \in \{J, H, K\}$. As in Section 2.1, we focus on color *difference*: we determine the earliest time, $t_\triangle$, at which

the colors of each rCCSN model differ from those of the unenriched model by at least one magnitude. Since this divergence occurs at a range of $R - X$, the focus on color difference rather than absolute color is useful for making comparisons across a diverse set of models. (However, we provide more concrete predictions of color itself in Sections 4.1.1 and 4.2.2.) To demonstrate the importance of the NIR bands, we perform the same calculation for the optical color $V - R$ and find no models for which $\Delta(V - R)$ is ever greater than 1 mag.

The top three panels of Figure 8 plot, as contours, t_Δ for $R - J$, $R - H$, and $R - K$. Models with high ψ_{mix} and high M_{rp} diverge from the r-process-free model earlier than models with less extreme enrichment parameters. This is consistent with earlier analytic arguments (e.g., Figure 3). The divergence also occurs sooner for $R - K$ than for $R - J$ or $R - H$. (Crucially, however, *any* choice of $R - X$ is a more reliable r-process indicator than optical colors, as seen in the bottom panel, which shows the maximum difference in $V - R$ for each model.)

Figure 8 also hints at when signs of more modest enrichment may appear; for $\psi_{\mathrm{mix}} \leqslant 0.3$, the color difference for all $R - X$ is <1 mag until ~2–3 months after explosion. In fact, for many $(M_{rp}, \psi_{\mathrm{mix}})$, $\Delta(R - X)$ does not exceed our threshold within the time frame of the simulation, or exceeds it for only one of the three colors considered.

Still, Figure 8 reinforces the potential of pre-nebular-phase observations for r-process detection. The dashed black curves in the top three panels show which rCCSNe, once their ejecta were fully transparent, would have $\Delta(R - X) = 1$ mag. (Here, in contrast to Figure 2, we have determined the nebular SED following the prescription of Section 3.2.) The swaths of parameter space that lie between the light-gray regions and the dashed lines contain models whose enrichment is more visible late in the photospheric phase, when at least the enriched core remains opaque, than during the nebular phase, after the emission has achieved its asymptotic colors.

4.1.1. Supernova Case Studies

We will argue later that, for questions of r-process detectability, classifying models based on M_{ej}, β_{ej}, and M_{56} is of limited utility. Regardless, before proceeding to a more observationally motivated schema, we present detailed color evolution predictions for a handful of models based on analyses of stripped-envelope SN demographics by Barbarino et al. (2021) and Taddia et al. (2019). (We note that many groups (Drout et al. 2011; Prentice et al. 2019; Perley et al. 2020) have contributed to efforts to uncover the distributions of SN Ic/Ic-BL properties, and that the characteristics of an "average" SN in a given category remain uncertain.)

In addition to cases representing typical SNe Ic/Ic-BL, we consider models based on individual SNe Ic-BL with inferred ejecta masses much higher and much lower than average, in order to explore how the signal may vary within the SN Ic-BL population. The explosion properties of our four models, along with the event or analysis on which each is based, can be found in Table 4. We enrich each of these models with 0.03 $M_\odot$ of r-process material, spread out to varying mixing coordinates ψ_{mix}.

Figure 9 shows the $R - X$ color evolution for each set of explosion parameters as a function of ψ_{mix}. We display for comparison the colors of an SN with the same explosion properties but no r-process enrichment. To better summarize the data, and to situate the r-process-induced changes in color
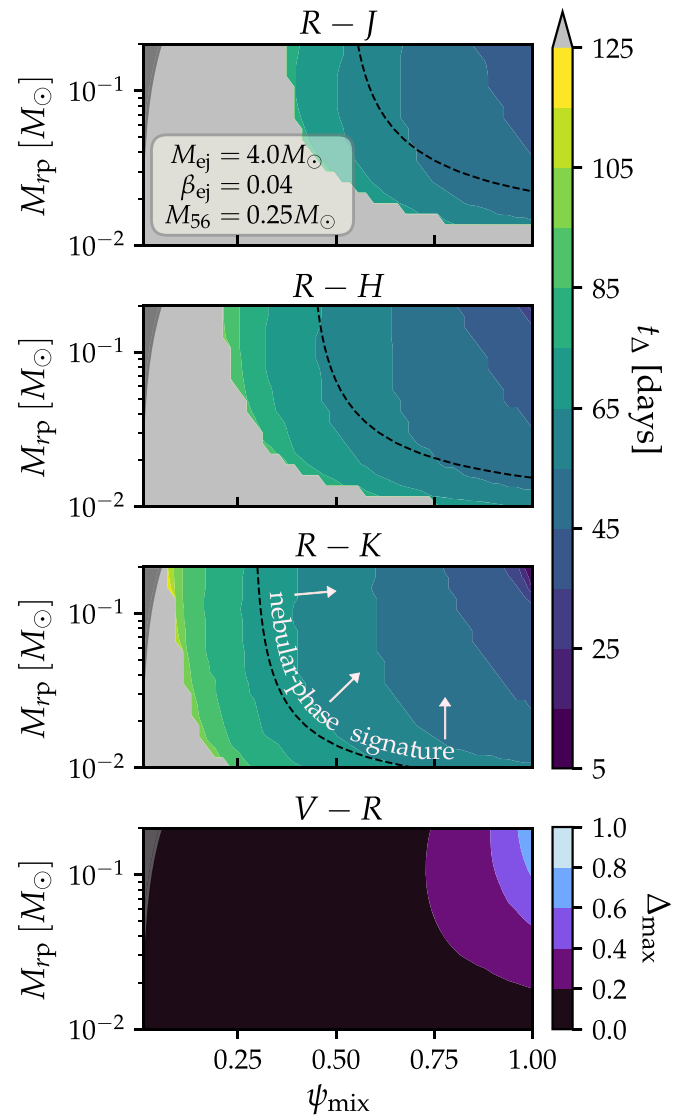

Figure 8. The effects of enrichment are strongest at redder wavelengths and when the r-process mass and/or the degree of mixing are high. Top three panels: the times (t_Δ) at which select colors of rCCSNe with variable M_{rp} and ψ_{mix} but uniform M_{ej}, β_{ej}, and M_{56} (=4.0 $M_\odot$, 0.04, and 0.25 $M_\odot$, respectively) first differ meaningfully ($\Delta \geqslant 1$ mag) from an unenriched SN with the same explosion parameters. The divergence occurs earlier for higher M_{rp} and ψ_{mix}, and for a larger fraction of the models as redder bands are considered. Models to the left of the dashed black lines in each panel are found, under the framework of Section 3.2, to have $\Delta(R - X) < 1$ mag once the ejecta is fully transparent and therefore meet our detection threshold only in the photospheric phase. Bottom panel: the maximum difference (with respect to time) in $V - R$ of the rCCSNe compared to the unenriched model. The effect is small in the optical bands; for no model does $\Delta(V - R)$ ever exceed 1 mag. All panels: dark gray shading marks parameter combinations disallowed by the requirement that r-process-enriched cores also contain ^{56}Ni ($\psi_{\mathrm{mix}}M_{\mathrm{ej}} \geqslant \psi_{\mathrm{mix}}M_{56} + M_{rp}$).

more directly in the context of observational SN properties, we also plot in the bottom row of Figure 9 the maximum color for each model and the time at which that maximum occurs, formulated as a multiple of the R-band rise time, $t_{R,\mathrm{pk}}$. We adopt this normalization because a given SN's time to peak defines the timescale on which it evolves; expressing times in terms of $t_{R,\mathrm{pk}}$ makes it easier to compare SNe with a range of characteristic durations.

Regardless of ψ_{mix}, the colors of the rCCSN models track those of their unenriched counterparts at early times, becoming

Table 4
Explosion Properties of the Models of Figure 9

Type	M_{ej} ($M_\odot$)	β_{ej}	M_{56}	Reference
Typical Ic-BL	3.97	0.044	0.33	T2019 [a] (average values)
High-mass Ic-BL	10.45	0.029	0.85	T2019 (PTF10ysd)
Low-mass Ic-BL	1.51	0.050	0.21	T2019 (PTF10tqv)
Typical Ic	3.97	0.020	0.21	B2021 [b] (average values)

Notes.
[a] T2019: Taddia et al. (2019).
[b] B2021: Barbarino et al. (2021).

noticeably redder only later on (around $t \gtrsim 25$ days for this set of transients). The extent of the reddening depends on ψ_{mix} and on M_{ej}, β_{ej}, and M_{56}; nevertheless, certain general trends are apparent.

While the effects of the r-process are present for all colors considered, they increase in prominence with the wavelengths of the NIR band. This theme is also apparent in the bottom panels of Figure 9. For all colors, models with at least moderate ψ_{mix} occupy a distinct region of parameter space compared to poorly mixed or unenriched models. The separation is strongest for $R - K$.

More than color, the signal strength depends on the explosion parameters, particularly velocity. R-process-induced changes in color are far more noticeable for the SN Ic-BL models with typical and low total ejecta masses (which have $\beta_{ej} = 0.044$ and 0.050, respectively) than for the typical SN Ic model or the SN Ic-BL with a higher ejecta mass (which have $\beta_{ej} < 0.03$). This can be seen in both the full color evolution and the position of each model in parameter space of the bottom panels.

However, consistent with Figure 8, the color change is most sensitive to the mixing coordinate ψ_{mix}. For nearly all models with $\psi_{mix} \geqslant 0.1$, r-process enrichment produces color extrema redder than the asymptotic colors of the corresponding unenriched SN. For some models, this is a global maximum occurring at a delay relative to the unenriched SN. This is the case for $\psi_{mix} \gtrsim 0.2$–0.3 for the typical and low-mass Ic-BL models and for $\psi_{mix} \gtrsim 0.4$ for the high-mass Ic-BL and the typical Ic model. (Even in the case of strong mixing, though, the difference between the enriched and unenriched SN colors is much smaller for the latter two cases than for the former two.)

At lower levels of mixing, the colors of the rCCSNe track those of their unenriched SN counterparts for a longer period of time and rise only to a local maximum after diverging. In these cases, as the bottom panels indicate, the maximum values of $R - X$ would not be sufficient to distinguish enriched from unenriched SNe; longer-term precision photometry would be required.

Nevertheless, it is reassuring that only the slowest and/or most poorly mixed models considered here fail entirely to form a distinct $R - X$ peak prior to the nebular phase. For typical SN Ic-BL explosion parameters, rCCSNe with $\psi_{mix} \geqslant 0.1$ exhibit either a global maximum $R - K$ color > 0 or a secondary maximum < 0 at 50 days $\lesssim t \lesssim 100$ days. In contrast, without enrichment we predict a peak value of $R - K = 0.2$ at $t = 40$ days. This again points to the value of pre-nebular-phase observations for evaluating collapsars as sites of r-production, particularly for $\psi_{mix} \geqslant 0.2$.

4.2. Prospects for Detection

While the discussion of Sections 4.1 and 4.1.1 is useful for illustrating trends, it may overstate the differences between r-process-rich and r-process-free SNe. Emission from models with large M_{rp} and ψ_{mix}—i.e., the models Figures 8 and 9 suggest should be easiest to identify—is likely to be so impacted by enrichment that it bears little resemblance to the emission from an r-process-free counterpart of the same M_{ej}, β_{ej}, and M_{56}. Since observers have no way of knowing a priori the physical properties of an SN explosion, a more appropriate reference case for an rCCSN—particularly if it is highly enriched or very well mixed—is an r-process-free SN with similar *observed* properties.

For the following analysis, we therefore categorize our models in terms of observable, rather than physical, parameters. Specifically, we classify them according to their R-band rise time, $t_{R,pk}$; peak R-band magnitude, M_R; and velocity, β_{ej}. (While β_{ej} is not an observed property in the same sense as $t_{R,pk}$ and M_R, measurements of absorption features in SN spectra can provide estimates of average ejecta velocities.) SNe (whether r-process-enriched or not) with comparable $t_{R,pk}$, M_R, and β_{ej} will not evolve in perfect synchronicity; still, this procedure allows us to at least compare models with similar behavior near peak light, when most observations are obtained.

Figure 10 demonstrates the advantage of this approach. Its histogram shows the diversity of M_R and $t_{R,pk}$ that characterize models with fixed explosion parameters—in this case, (M_{ej}, β_{ej}, M_{56}) = (4.0 $M_\odot$, 0.04, 0.25 $M_\odot$)—but variable M_{rp} and ψ_{mix}. If r-process material is present, the enrichment parameters (M_{rp} and ψ_{mix}) influence the properties of the light curves. More than 30% of the models in Figure 10 have a $t_{R,pk}$ (M_R) that differs from the r-process-free case by more than 1 day (0.5 mag). This highlights the risk of assuming that M_{ej}, β_{ej}, and M_{56} can be extracted from light-curve data independent of the amount (or existence) of r-process enrichment.

However, a challenge of this framework is that there is no way to identify a single r-process-free model to which an rCCSN model should be compared. (Unlike M_{ej}, β_{ej}, and M_{56}, we cannot force ordinary SNe and rCCSNe to have the same $t_{R,pk}$ and M_R.) As in earlier sections, we focus on color as a diagnostic and continue to use $\Delta(R - X) \geqslant 1$ mag as the criterion for detectability, with $X \in \{J, H, K\}$. Now, however, instead of making one-to-one comparisons, we sort our models into bins of size $\Delta t_{R,pk} = 2$ days, $\Delta M_R = 0.25$ mag, and $\Delta\beta_{ej}/\beta_{ej} = 0.37$ and then contrast the colors of individual rCCSNe with an average color evolution constructed from the r-process-free SNe in the same bin.

This introduces some uncertainty into the comparison, as unenriched models in a given bin do not produce identical SNe. Indeed, the time-dependent standard deviation of the $R - X$ colors for r-process-free SNe, $\sigma_{R-X}(t)$, can reach ~ 0.7 mag at certain times for certain bins. However, σ_{R-X} depends on velocity. This can be seen in Figure 11, which presents the cumulative distribution function of the maximum σ_{R-X} for bins with a particular β_{ej}. For bins corresponding to typical SN Ic/Ic-BL velocities ($0.03 \lesssim \beta_{ej} \lesssim 0.1$), $\sigma_{R-X} < 0.5$ mag at all times for all X considered. Moreover, in this same velocity range, the average bin has at all times $\sigma_{R-X} \lesssim 0.25$ mag, much less than our detection threshold $\Delta(R - X) \geqslant 1$. This increases our confidence that models flagged as detectable truly do differ in significant ways from the unenriched reference cases.
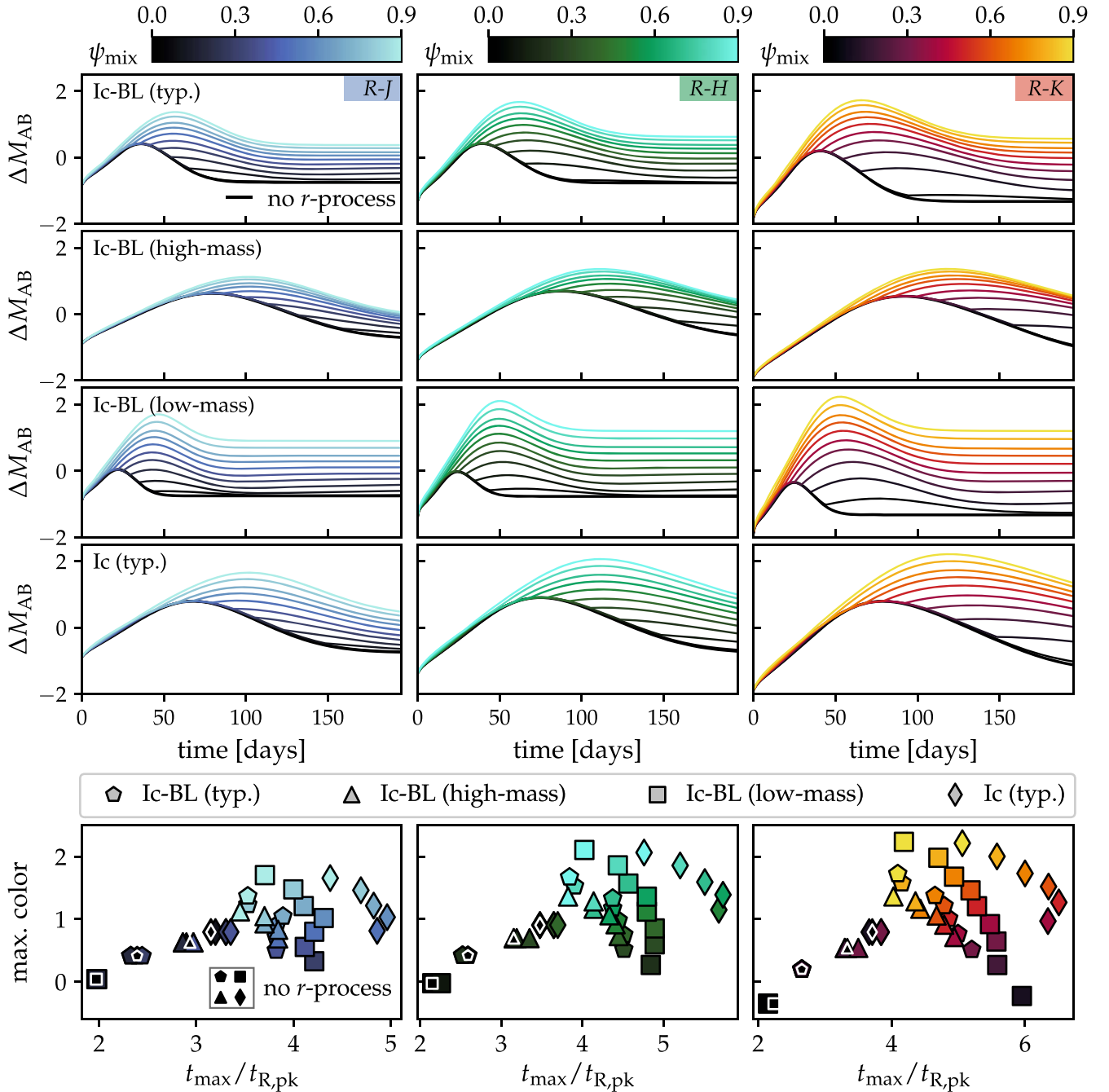
Figure 9. The effect of *r*-process enrichment ($M_{rp} = 0.03\ M_{\odot}$, variable ψ_{mix}) on $R - X$ for four explosion models with M_{ej}, β_{ej}, and M_{56} corresponding either to literature-reported averages or to particular events representing extrema in the distribution of inferred SN Ic-BL properties (see Table 4 for details). We show the full color evolution for each model (top panels), as well as the maximum color and the time at which it occurs (bottom panels). In all panels, we plot predictions for *r*-process-free models with the same explosion properties for comparison. For all but the lowest ψ_{mix}, the presence of *r*-process material enhances $R - X$, producing either a secondary maximum or a delayed global maximum relative to the unenriched cases. Significantly, the strongest enhancement can be transient in nature and may occur well before the *r*CCSN reaches its asymptotic colors. The impact is strongest for the highest-velocity models (the typical and low-mass SNe Ic-BL) but can be significant even for a typical SN Ic if ψ_{mix} is high.

An additional complication is the fact that enriched and ordinary SNe do not populate the exact same regions in the $t_{R,pk}$ $-M_R-\beta_{ej}$ parameter space. In the few instances where *r*CCSNe occupy a bin containing no unenriched SNe, we prioritize comparing events of similar $t_{R,pk}$ and M_R, since these are directly measured, while β_{ej} must be inferred from observations. In these cases, we define the reference color evolution for the calculation of $\Delta(R - X)$ by selecting, from all the *r*-process-free SNe within the empty bin's range of $t_{R,pk}$ and M_R, those

with velocities closest to the empty bin's central velocity and averaging over that subset. If there are no *r*-process-free SNe (of any velocity) in the desired bin in $(t_{R,pk}, M_R)$, we do not calculate $\Delta(R - X)$.

4.2.1. Minimum Observable Mixing Coordinate

Having established a new method for comparing enriched and unenriched SN models, we return to the *r*CCSNe and
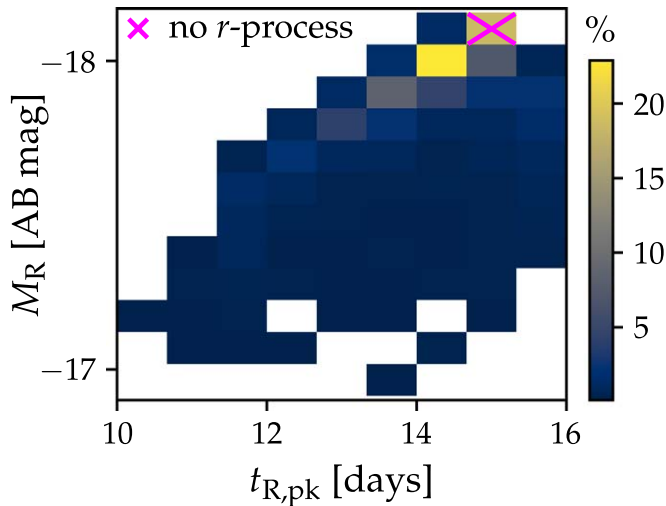
Figure 10. The presence of *r*-process material alters the SN light curves even near optical peak. As a result, *r*-process-free models with matching explosion parameters are not necessarily ideal points of comparison for *r*CCSNe. Above, we show how models with fixed $(M_{\rm ej}, \beta_{\rm ej}, M_{56}) = (4.0\ M_\odot, 0.04, 0.25\ M_\odot)$ are distributed in $t_{R,\rm pk}$ and M_R, where $t_{R,\rm pk}$ (M_R) is the rise time (peak magnitude) in R band. The histogram cell containing the *r*-process-free model with the same $M_{\rm ej}$, $\beta_{\rm ej}$, and M_{56} is marked with a fuchsia cross. It contains only a minority of the enriched models.
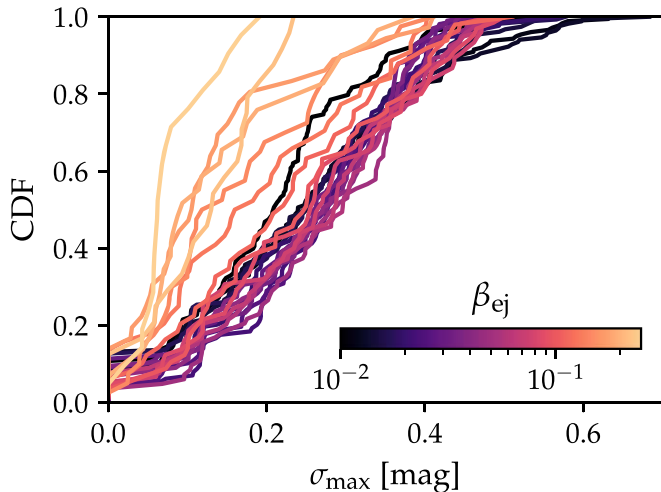
Figure 11. SNe with similar observed properties near peak do not exhibit perfectly uniform color evolution. Having binned the *r*-process-free SNe according to $t_{R,\rm pk}$, M_R, and $\beta_{\rm ej}$ and averaged their $R - X$ color evolution, we determine $\sigma_{\rm max}$, the maximum standard deviation in each bin for any $R - X$, with respect to time. The cumulative distribution function of $\sigma_{\rm max}$ is shown above for bins of constant central $\beta_{\rm ej}$. For typical SN Ic/Ic-BL velocities ($0.03 \lesssim \beta_{\rm ej} \lesssim 0.1$), most bins have $\sigma_{R-X} \lesssim 0.4$ mag at all times, less than our *r*-process detection threshold $\Delta(R - X) \geqslant 1$ mag. Furthermore, $\sigma_{\rm max}$ is not necessarily indicative of σ_{R-X} when a detection occurs (i.e., when $\Delta (R - X) \geqslant 1$ mag). In practice, the uncertainty at these times is often much less than the maximum value.

determine, as a function of $t_{R,\rm pk}$, M_R, and $\beta_{\rm ej}$, the minimum mixing coordinate that produces a detectable signal. We define this minimum, $\psi_{\rm min}$, as the value of $\psi_{\rm mix}$ for which $\geqslant 50\%$ of models in a given bin satisfy $\Delta(R - X) \geqslant 1$ mag before some threshold time, with the threshold time a parameter of the calculation.

We find that $\psi_{\rm min}$ depends primarily on the ejecta velocity $\beta_{\rm ej}$ of the rCCSNe, the time frame over which observations are carried out, and the color considered (i.e., the choice of X). The

effect of each of these is illustrated in Figure 12, which shows $\psi_{\rm min}$ for each bin, or, for bins in which no $\psi_{\rm mix}$ qualified as detectable, the maximum $\psi_{\rm mix}$ represented in the bin. For simplicity, we present in Figure 12 slices from the parameter space; each panel corresponds to one observation time frame, one choice of X, and one (bin-centered) $\beta_{\rm ej}$. We have also restricted the models of Figure 12 to those with $M_{\rm rp} = 0.03\ M_\odot$. However, the same trends apply to other choices of $M_{\rm rp}$.

As expected from the discussion of Section 2.2 (e.g., Figure 4), the top row of Figure 12 shows that *r*-process signatures are more easily detected for *r*CCSNe with higher $\beta_{\rm ej}$. Higher $\beta_{\rm ej}$ values characterize SNe associated with the GRBs that serve as indirect evidence of the accretion disks predicted to support *r*-process production. This means that the most straightforward version of the *r*-process collapsar hypothesis, in which an accretion disk wind injects *r*-process elements into a high-velocity SN, should be the easiest to test. On the other hand, alternate modes of *r*-production in SNe, such as lower-energy "failed-jet" SNe (Grichener & Soker 2019) or neutrino-driven winds from newly born magnetars (Vlasov et al. 2017; Thompson & ud-Doula 2018), will be more difficult to evaluate.

While incomplete mixing and slower expansion velocities hinder *r*-process detection, observing strategy can at least partially compensate. The middle row of Figure 12 demonstrates that extending observations to later times increases the likelihood of a detection, even for models with lower $\psi_{\rm mix}$. For *r*CCSNe with $\beta_{\rm ej} \approx 0.06$, we find that *r*-process signals are not reliably detected in $R - H$ at times $\leqslant 2t_{R,\rm pk}$, even if mixing is extensive. (Nearly all bins in the middle row contain models with $\psi_{\rm mix} = 0.9$.) In contrast, for $t \leqslant 4t_{R,\rm pk}$ ($6t_{R,\rm pk}$), $\psi_{\rm min} \leqslant 0.3$ for 31% (46%) of the bins. That said, according to our definition, a successful detection implies only that a color difference $\Delta(R - X) \geqslant 1$ mag is obtained *at some point* during the observation; it reveals nothing about the duration of that signal. Thus, cadence is also important.

Finally, as can be seen in the bottom row of Figure 12, the passbands chosen for the color comparison also matter. We find that *r*-process detection for minimally mixed ejecta is easier for $R - K$ than $R - H$ and $R - J$. However, particularly if observations are limited to photometry, multiple NIR bands may be required to rule out spurious emission features unrelated to *r*-process enrichment (e.g., overtones of carbon monoxide; Gerardy et al. 2002). In that sense, detection prospects may be limited by the performance of the weakest color considered.

Not included in Figure 12 is the effect of *r*-process mass, which we find has a comparatively minor impact on the minimum detectable mixing coordinate. In Figure 13, we show $\psi_{\rm min}$ for models with bin center $\beta_{\rm ej} = 0.06$ (the fiducial velocity of Figure 12), $t_{\rm obs} \leqslant 4t_{R,\rm pk}$, and two *r*-process masses, $M_{\rm rp} = 0.03$ and $0.15\ M_\odot$. We calculate $\psi_{\rm min}$ based on the $R - K$ color, for which the effects of *r*-process enrichment are strongest.

Despite the fivefold increase in $M_{\rm rp}$, values of $\psi_{\rm min}$ are fairly stable. In part because of the velocity dependence described above, the greatest gains in detectability are for fast-evolving transients ($t_{R,\rm pk} \approx 5$–10 days), for which $\psi_{\rm min}$ falls from $\simeq 0.2$ to $\simeq 0.1$. For events with longer rise times, even a large $M_{\rm rp}$ is invisible except in cases of strong mixing.

The insensitivity of $\psi_{\rm min}$ to $M_{\rm rp}$ is due to the high opacity of *r*-process material relative to the unenriched ejecta and to the dominance of ^{56}Ni as an energy source in our model. Because
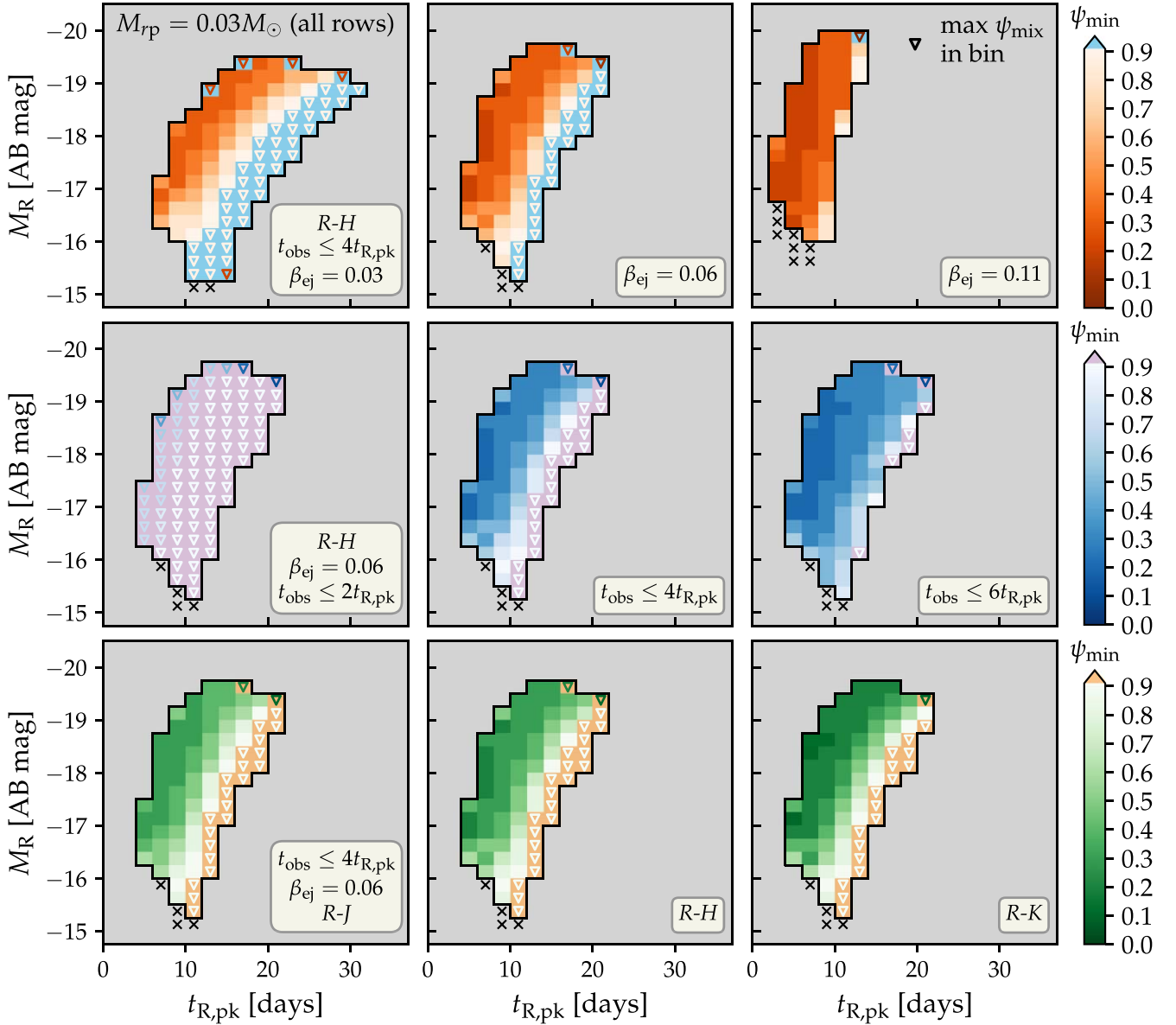
Figure 12. The minimum observable mixing coordinate, $\psi_{\min}$, depends on the intrinsic properties of the rCCSN and on the timescale and passbands of the observation. As elsewhere, an observable signal is one that produces an $R - X$ color difference of at least 1 mag compared to an average of unenriched SNe in the same bin ($\beta_{\rm ej}$, $t_{R,\rm pk}$, M_R) at some point during the observation time frame. We define $\psi_{\min}$ as the minimum $\psi_{\rm mix}$ for which $\geqslant 50\%$ of models in a bin are observable. In bins where no $\psi_{\rm mix}$ meet this criterion, an inverted triangle indicates the maximum $\psi_{\rm mix}$ within the bin. Black crosses indicate that a bin contained rCCSNe, but no unenriched SNe for comparison. All enriched models have $M_{r\rm p} = 0.03\,M_\odot$. Top panels: the effect of $\beta_{\rm ej}$. More deeply buried r-process material is more easily observed for faster expanding rCCSNe. Middle panels: the effect of observing time frame. If observations are restricted to times close to peak, the differences between enriched and unenriched SNe are difficult to discern, even for highly mixed ejecta. Prolonged observing campaigns provide more opportunities for detection. Bottom panels: the effect of passband. The signal is more easily observed when redder bands are considered in color calculations.

$\kappa_{r\rm p} \gg \kappa_{\rm sn}$, core ejecta polluted with even trace amounts of r-process elements acquires an opacity much higher than that of the surrounding envelope. Although increasing $M_{r\rm p}$ in the enriched core further enhances the opacity, the opacity difference between enriched and unenriched ejecta is larger than that between minimally and highly enriched ejecta. In this way, the effects of $\kappa_{r\rm p}$ diminish with increasing $M_{r\rm p}$. Moreover, even for high $M_{r\rm p}$, ^{56}Ni supplies most of the radioactive energy to the core, and raising $M_{r\rm p}$ does not meaningfully alter the energy budget of the enriched layers. Were the reverse true, increasing $M_{r\rm p}$ would cause the r-process-rich layers to shine more brightly (at NIR wavelengths) and, presumably, would produce a tighter correlation between $M_{r\rm p}$ and $\psi_{\min}$.

4.2.2. Colors and Timescales

In order to make our analysis more concrete, we next explore the color evolution of a subset of our model suite. As in Section 4.2.1, we categorize the models according to their R-band rise times and maxima, $t_{R,\rm pk}$ and M_R. We focus on rCCSNe of velocity $\beta_{\rm ej} = 0.06$ (typical for the SNe Ic-BL most likely to produce r-process elements in disk outflows) and a moderate level of mixing, $\psi_{\rm mix} = 0.3$. We use the same binning procedure as in Section 4.2.1 .

For each model, we find the earliest time, $t_{\rm RX2}$, at which $\Delta(R - X) \geqslant 1$ mag for at least two $X \in \{J, H, K\}$. (As before, the color difference is calculated with respect to an average of unenriched SNe in the same bin.) We adopt the more stringent,
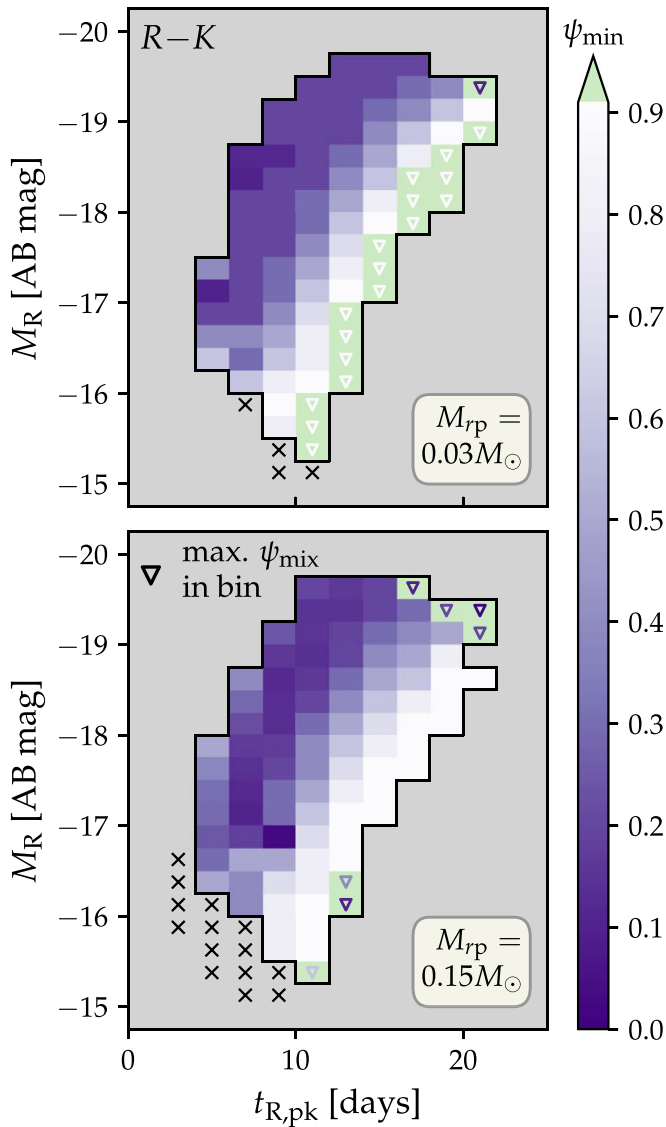
Figure 13. The same as Figure 12, but showing the impact of the r-process mass M_{rp} on $\psi_{\min}$, for fixed $\beta_{\rm ej} = 0.06$ and observing window $t_{\rm obs} \leqslant 4t_{R,\rm pk}$. Detectability is determined with respect to $R - K$. The minimum detectable mixing coordinate ($\psi_{\min}$) is largely insensitive to the quantity of r-process material, at least within the range of M_{rp} we consider; a factor of five increase in M_{rp} produces only a modest reduction in $\psi_{\min}$.

two-color standard to protect against false positives due to, e.g., emission features that affect the flux in only one band. However, we acknowledge that this stricter criterion will in general be met at later times, when finite (and band-dependent) detector sensitivities pose more of a challenge for observations. In addition to $t_{\rm RX2}$, we also record $R - K$ at $t = t_{\rm RX2}$, which we denote $(R - K)_{\rm RX2}$. This establishes for every model a characteristic timescale and $R - K$ color associated with r-process enrichment signals.

In Figure 14, we present for different M_{rp} the latest $t_{\rm RX2}$ and the lowest value of $(R - K)_{\rm RX2}$ in each bin. (We note that the model associated with the latest time is not necessarily also associated with the lowest color.) In other words, the grids of Figure 14 can be read as saying that an rCCSN with the specified parameters should produce a signal with $R - K$ at least as red as the indicated color by no later than the indicated time.

The r-process signal appears first for rCCSNe that are fast evolving and/or bright. In extreme cases ($t_{R,\rm pk} \lesssim 10$ days), the signal appears within ∼20 days, or ∼$2t_{R,\rm pk}$, and is associated with a moderate $R - K \approx 0.5$ mag. For low M_{rp}, these fast/bright rCCSNe are the only ones that meet our two-band criterion. For higher M_{rp}, detections happen over a broader swath of the parameter space. Detections in events with higher $t_{R,\rm pk}$ and lower M_R occur much later (75–100 days after explosion) but produce stronger $R - K$ colors (≈ 1mag).

While the details of Figure 14 depend on the choice of $\psi_{\rm mix}$ and $\beta_{\rm ej}$, the results nonetheless suggest that, absent a high degree of mixing, minimal r-process enrichment ($M_{rp} \lesssim 0.03$ $M_\odot$) will be difficult to detect except in the fastest-evolving transients. In contrast, if r-production occurs at a higher level (as SBM19 argued based on the presumed more massive accretion disks formed in collapsars vis-à-vis NSMs), a signal should be visible for a much wider range of observational parameters.

Though the quantity of r-process material determines the breadth of the parameter space over which a detection is feasible, Figure 14 suggests that it may be difficult, once a detection *is* made, to precisely constrain the r-process mass M_{rp}. More specifically, it appears that a detection can more easily be used to derive a lower limit for M_{rp} than an upper limit.

However, longer-term monitoring can provide additional information, allowing a better estimate of the r-process mass produced in a given rCCSN. In Figure 15, we show, for the same models represented in Figure 14 ($\beta_{\rm ej} = 0.06$, $\psi_{\rm mix} = 0.3$), the time at which the rCCSN reaches a maximum in $R - K$ and the value of that maximum. While we do not apply any criterion for $\Delta(R - X)$ in calculating these quantities, when determining $(R - X)_{\max}$, we consider only times after the photosphere has reached the r-process layers, ensuring that our color maxima are associated with the enriched ejecta. As a result, in some cases the maxima identified in Figure 15 are *local* rather than *global* extrema.

For bins in which detections are possible for multiple values of M_{rp} (in each panel, light-colored hatching indicates the regions where r-process signatures are not detectable according to the two-color standard established for Figure 14), increasing M_{rp} results in a higher maximum $R - K$, occurring at a later time. Thus, while the r-process mass, at least in this mixing regime, has a small effect on the signal in its earliest stages, diligent photometric follow-up may still successfully constrain M_{rp}. In fact, the relative insensitivity of the early characteristics of the signal to M_{rp} may be an advantage, as it decouples the determination of ideal observing strategies from assumptions about the level of r-production in collapsars.

4.3. Formulating Observing Strategies

As we have seen, even for SNe with optimal explosion properties, the odds of confidently detecting r-process signatures depend on the observing strategy employed. The observing window and the bands selected are particularly important. If we require for detection a color difference of at least 1 mag for at least two colors $R - X$, we find that 48% of our rCCSN models with SN Ic-BL-like velocities ($0.05 \leqslant \beta_{\rm ej} \leqslant 0.1$) are detectable before $t = 50$ days if the chosen colors are $R - J$ and $R - K$. This percentage encompasses all mixing coordinates and smooths over considerable variation with $\psi_{\rm mix}$.
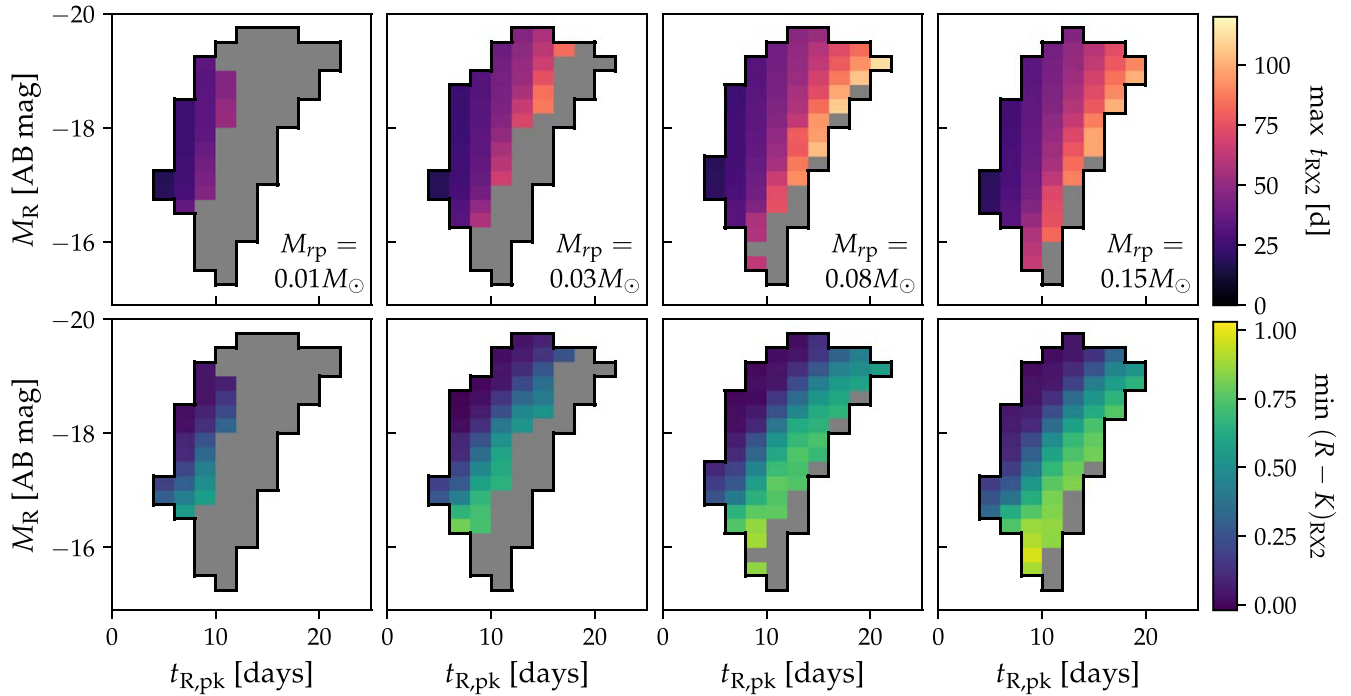
Figure 14. The range of timescales and colors associated with an r-process detection for rCCSNe with $\beta_{ej} = 0.06$, a moderate $\psi_{mix} = 0.3$, and different values of M_{rp}. For each model, we find the earliest time, t_{RX2}, at which an $R - X$ color difference (relative to unenriched SNe) of $\geqslant 1$ mag occurs for at least two X in the NIR bands (J, H, and K). We also record $R - K$ at $t = t_{2RX}$. We display the maximum t_{RX2} (top panels) and the minimum $(R - K)_{RX2}$ (bottom panels) in order to provide a conservative estimate of the strength and timing of the signal. Bins in which no models achieved $\Delta(R - X) \geqslant 1$ for two X are colored gray. Evidence of the r-process emerges sooner and is associated with bluer $R - K$ for rCCSNe with lower $t_{R,pk}$ and, to a lesser extent, brighter M_R. The value of M_{rp} primarily influences where in $t_{R,pk} - M_R$ space a signal is detectable; it has only a minor effect on t_{RX2} and $(R - K)_{RX2}$.

If we consider only rCCSNe with $\psi_{mix} \geqslant 0.6$, 74% are detectable, while for $\psi_{mix} < 0.3$ that value drops to 0.5%.

Observing in redder bands improves the situation, as does extending the observing period. If $R - H$ and $R - K$ are instead used for the color comparison, 58% of the high-velocity models are detectable by $t = 50$ days, and 65% by $t = 80$ days. If we again differentiate by ψ_{mix}, we find that 14% of the poorly mixed models and 79% of the well-mixed models are detectable by $t = 50$, and 17% and 85%, respectively, by $t = 80$.

Lower-velocity rCCSNe pose a greater challenge. Of models with $\beta_{ej} < 0.05$, r-process signatures are visible for only 10% before day 50, even when $\Delta(R - X)$ is calculated with respect to $R - H$ and $R - K$. The percentage is a dismal 1% for models with $\psi_{mix} < 0.3$ and rises to only 15% for $\psi_{mix} \geqslant 0.6$.

To clarify these trends, we show in Figure 16 the fraction of rCCSN models of different ψ_{mix} that satisfy a two-color detection criterion before a given time. Consistent with the discussion above, we divide our models into low-velocity ($0.01 \leqslant \beta_{ej} < 0.05$) and high-velocity ($0.05 \leqslant \beta_{ej} \leqslant 0.1$) subsets and consider the effect of the colors used to calculate $\Delta(R - X)$.

While Figure 16 shows that only a limited fraction of enriched models are detectable under this framework, it also identifies the period most likely to yield a successful detection, *if* one is to be forthcoming. For example, considering rCCSNe with higher β_{ej} (i.e., the top two panels), nearly all models that become detectable within our simulation time frame are detectable by $t = 70$ days post-explosion. In contrast, the detectable fraction of lower-velocity models continues to rise steadily well past $t = 100$ days. (We caution that while these quoted percentages reveal important relationships between observing strategies and the ability to discern r-process-enrichment signatures, their exact values depend

on the distribution of explosion and enrichment parameters in our model suite, which does not necessarily reflect the distributions within the cosmological population of SNe Ic/Ic-BL. Rather than the percentage of rCCSNe that can be identified by a certain observation, they more accurately measure the fraction of the parameter space an observation can probe.)

Observing r-process signatures in poorly mixed explosions will be challenging regardless of other factors; still, Figure 16 suggests that the odds of success will be maximized if high-velocity targets are followed up in multiple bands—ideally including multiple NIR bands covering the reddest wavelengths possible—for at least 2 months after explosion. By $t \approx 2.5$ months, the odds that a signal will appear for the first time decline steeply. If no signal has been detected by this point, observing resources would be better spent on new targets.

What Figure 16 does not elucidate is the cadence of observations needed to catch r-process signals, which are often transient. To provide some sense of the signals' longevity, we calculate the fraction of models that are *instantaneously* detectable as a function of time, as well as the distribution of signal lifetimes, Δt_{sig}. Here, as elsewhere, "detectability" refers only to the color difference relative to an r-process-free SN baseline; we do not consider telescope sensitivity, or other technicalities that would in practice constrain the acquisition of data. We show the results in Figure 17 for rCCSNe with $0.05 \leqslant \beta_{ej} \leqslant 0.1$, for a signal constituted by $\Delta(R - X) \geqslant 1$ mag with $X = H$ and K. (In other words, we selected the SNe and the $R - X$ colors that favor detection.) The top panel shows the fraction of models, as a function of ψ_{mix}, detectable at a given time, while the bottom panel shows the fraction of models, $f_>$, with a signal lifetime exceeding a given duration Δt_{sig}.
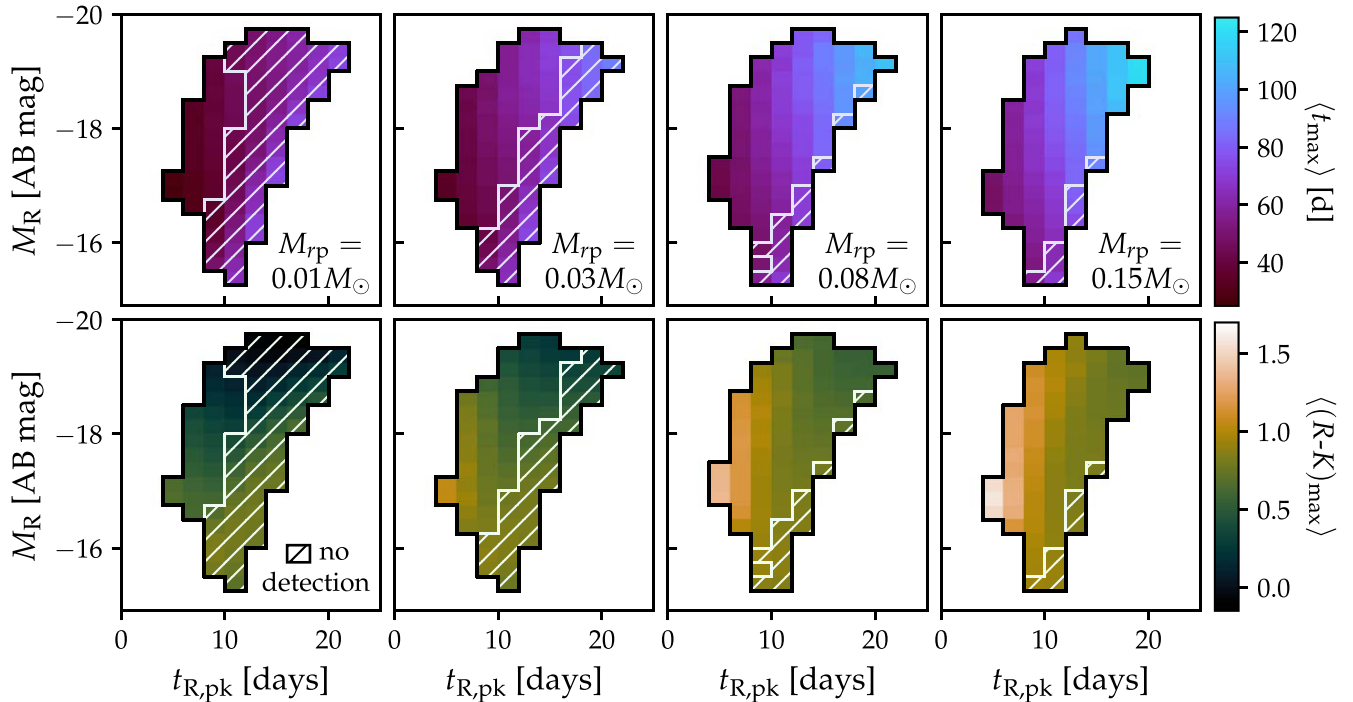
Figure 15. The maximum $R - K$ color recorded for rCCSNe with $\beta_{ej} = 0.06$, $\psi_{mix} = 0.3$, and different r-process masses M_{rp}, after the r-process-free envelope has become optically thin. We show the bin-averaged values of both the color maxima (top panels) and the times at which they occur (bottom panels). In all panels, hatching indicates bins for which no models have $\Delta(R - X) \geqslant 1$ for at least two bands $X \in \{J, H, K\}$ at any point before $t = 200$ days. In bins for which detections are possible for multiple r-process masses, the maximum $R - K$ increases with M_{rp}, as does the time at which that maximum takes place. This suggests that long-term photometric follow-up can provide better constraints on M_{rp} than an initial detection alone.

A large fraction of well-mixed models are detectable starting at $t \sim 30$ days and remain detectable thereafter; of models with $\psi_{mix} \gtrsim 0.5$, $\lesssim 60\%$ are detectable over a period of $\geqslant 100$ days. For lower mixing coordinates, the epoch at which the largest fraction of models is detectable is similar (~ 50 days after explosion), but that fraction is lower, and Δt_{sig} decreases in concert with ψ_{mix}. For example, while 47% of models with $\psi_{mix} = 0.3$ have signals lasting $\Delta t_{sig} \geqslant 30$ days, only 13% of those with $\psi_{mix} = 0.2$ do. Figure 17 suggests that long-lived signals enduring out into the nebular phase can be expected in a majority of cases only if $\psi_{mix} \gtrsim 0.5$.

Taken together, Figures 16 and 17 indicate that observations targeting high-velocity SNe in the first few months after explosion and at reasonably high cadence will maximize the chances of identifying rCCSNe. The most poorly mixed rCCSNe that offer any hope of detection (those with $\psi_{mix} = 0.1$) have signal durations sharply concentrated at $\Delta t_{sig} \lesssim 25$ days. Ideally, observing campaigns would return to such a target multiple times during this window to maximize confidence in a detection, suggesting a delay of no greater than ~ 1 week (and optimally ~ 3–4 days) between consecutive visits.

5. Conclusions

Our analysis suggests that it may be possible to directly detect signs of the r-process in photometric data from rCCSNe. Significantly, observations can constrain r-process enrichment at a level that would make collapsars competitive with NSMs as r-process sources. (While the exact mass per event required for collapsars to overtake mergers depends on the uncertain rates of NSMs, NS-black hole mergers, and GRB-SNe, we estimate (e.g., Siegel et al. 2019; Brauer et al. 2021) that

$\langle M_{rp} \rangle \approx 0.01$–$0.1\ M_\odot$ would put collapsars in contention.) In contrast, observations of this kind are not suitable for probing the much less efficient r-production ($M_{rp} \lesssim 10^{-5}$–$10^{-4}\ M_\odot$; e.g., Qian & Woosley 1996) that may occur in some CCSNe whose pre-collapse angular momentum is insufficient to support the formation of an accretion disk. The inadequacy is even starker if noncollapsar CCSNe synthesize lighter r-process elements with lower opacities.

Though previous studies (SBM19) advocated testing the r-process collapsar hypothesis with observations during the nebular phase, we find that, in many cases, the r-process signal manifests much earlier in the rCCSN's evolution. Thus, in addition to being an important tool for the discovery of rCCSNe in its own right, photospheric-phase observation can also identify the events most worthy of follow-up in the nebular phase. Such triage is particularly important given that nebular-phase observations are resource intensive, and the tool best suited to take them—the Mid-Infrared Instrument (MIRI) aboard the James Webb Space Telescope (JWST)—will have limited availability for rapid-response, target-of-opportunity campaigns. Early identification will thus maximize the science returns from what will likely be a finite number of visits to candidate rCCSN nebulae.

Because our models are not fully mixed, their photospheric phase consists of an early optical stage bright and long-lived enough that, in most cases, its (optical) peak magnitude and rise time are consistent with those of observed SNe (e.g., Figure 12). This means that rCCSNe are—except in extreme cases—likely to be found in blind searches and confidently identified as SNe Ic/Ic-BL. After this initial period, which is powered by the r-process-free outer envelope, rCCSN emission becomes dominated by radiation from the r-process-enriched
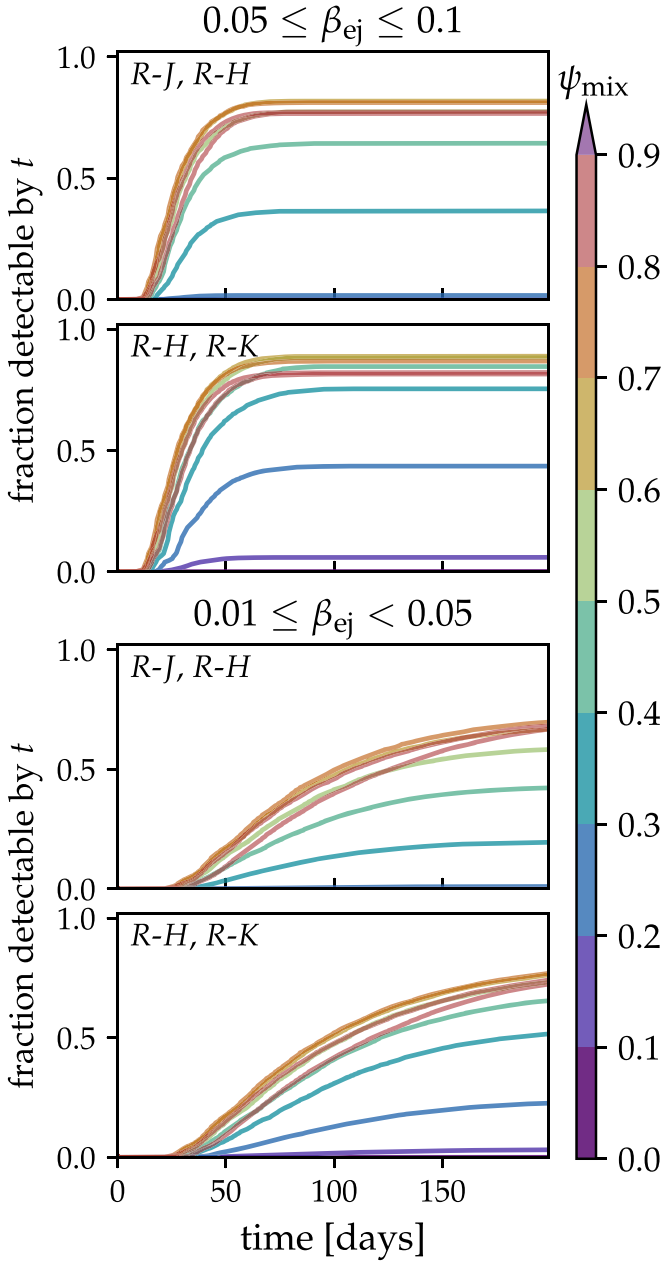
Figure 16. The time frame, relative to explosion, required to constrain r-process production in collapsars depends on the properties of the rCCSN and on the bands used in the observation. Above, we show the cumulative fraction of models that have been observable, according to a two-color criterion, at any point before time t. We have coarsely binned the models in β_{ej} and broken them down by mixing coordinate ψ_{mix}. For higher-velocity rCCSNe (top panels), while detectability is particularly sensitive to ψ_{mix}, most of the detectable models reveal themselves within ~2 months of explosion. In contrast, the odds of a detection for lower-velocity rCCSNe (bottom panels) rise continually out to $t = 200$ days, when our simulations end. Regardless of velocity, color comparisons in $R - H$ and $R - J$ offer better prospects for detection than $R - J$ and $R - H$, particularly for models with lower ψ_{mix}.

core. Due to the high opacity of r-process elements, the signal at this point appears as an NIR excess and is most clearly distinguishable by its optical−NIR colors.

Multiband photometry extending out to late times and long wavelengths (ideally including K band) is therefore critical in the hunt for rCCSNe. The most promising targets are highly kinetic GRB-SNe/SNe Ic-BL. Not only are these the SNe most closely tied, theoretically, to the collapsar model of the
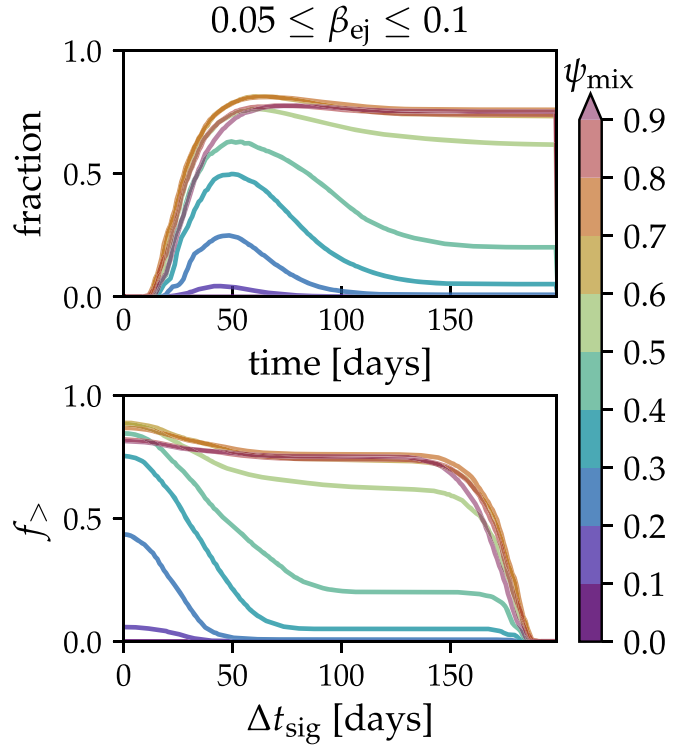

Figure 17. The ideal observing cadence depends on Δt_{sig}, the lifetime of the signal, which is sensitive to the mixing coordinate ψ_{mix}. We focus here on rCCSNe with high velocities and define detectability as $\Delta(R - X) \geqslant 1$ for $X = H$ and K. Top panel: the fraction of models detectable at a particular time since explosion, for different ψ_{mix}. Regardless of ψ_{mix}, the fractions reach their peak around 50 days. (However, the values of those peaks *do* depend on ψ_{mix}.) Bottom panel: the fraction of models, $f_>$, that have a signal duration $\geqslant \Delta t_{sig}$, as a function of mixing coordinate ψ_{mix}. For well-mixed models, Δt_{sig} can exceed 100 days, while signals for models with lower ψ_{mix} are more ephemeral.

r-process, but they are also characterized by rapid expansion that causes any r-process-free outer layers to quickly become transparent, revealing the inner, enriched core on a fairly short timescale. (Crucially, however, the signal is delayed enough that contamination by an afterglow—in the case of SNe Ic-BL discovered through a long GRB trigger—is not a concern.)

As we argued in Section 4.3, frequent monitoring of these high-velocity SNe in optical and at least H and K bands for the first ~75 days after explosion is an efficient strategy for rCCSN searches. While such an observation will not catch all rCCSNe, its misses will primarily be due to the intrinsic difficulty of identifying r-production in cases of minimal ψ_{mix}, and not to an insufficiently long observing window, or reliance on non-optimal colors to differentiate enriched from unenriched SNe.

The potential of such an observing strategy was recently demonstrated by an effort—the first of its kind—to systematically follow up SNe Ic-BL in the NIR in pursuit of photometric r-process-enrichment signatures. The observations, to be presented in a companion paper (S. Anand et al. 2022, in preparation), show evidence for diverse r-process-enrichment outcomes in these energetic SNe. Upcoming surveys by facilities with extensive infrared capabilities, e.g., WINTER (Lourie et al. 2020) and the Roman Space Telescope (Mutchler et al. 2021), will provide new opportunities to search for rCCSNe, while multiband follow-up of future gravitational-wave-detected kilonovae (e.g., Chase et al. 2022) will clarify the r-process contributions of NSMs.

Our ability to identify rCCSNe at even low levels of mixing will improve as our understanding of late-time SN emission solidifies. Regardless of the parameters of an observation and the properties of its target, a detection requires a clear picture of NIR emission from unenriched SNe in the nebular phase, against which new observations can be compared. We constructed our models of ordinary SNe using the limited data available. However, further observations of SNe Ib/c over the course of their evolution, with a focus on lower-energy events less likely to undergo an r-process, are necessary to more firmly establish baseline expectations of colors in the r-process-free case.

Nebular-phase r-process emission is another area where additional data would increase confidence in the models and, perhaps, inform observing strategies. If, for example, r-process nebulae shine predominantly at longer wavelengths than predicted by Hotokezaka et al. (2021, the study on which our models are based), emission even in J, H, and K bands could be negligible (Figure 5), and facilities with MIR capabilities may be required for smoking-gun detections in the nebular phase. It will also be important to ensure that dust, which is a known source of reddening in SNe (e.g., Szalai et al. 2019), is not the cause of any observed changes in $\{R - X\}$ colors. While the low densities resulting from the relatively low ejecta masses and high velocities that characterize SNe Ic-BL will work against dust formation and limit its impact on the spectrum (Liljegren et al. 2022), spectral measurements will be required to rule out a molecular source for emission in the the NIR and MIR.

Despite these uncertainties, taken as a whole, our findings suggest that signs of enrichment in rCCSNe may be visible across a significant fraction of the parameter space, which makes SN observation an important tool for assessing collapsars as sites of r-process nucleosynthesis. Observations of additional SNe Ic/Ic-BL and—one hopes—additional kilonovae will further refine this tool, providing a new method to uncover the means by which the universe becomes seeded with the heaviest elements.

ORCID iDs

Jennifer Barnes ⬤ https://orcid.org/0000-0003-3340-4784
Brian D. Metzger ⬤ https://orcid.org/0000-0002-4670-7509

References

Abbott, B. P., Abbott, R., Abbott, T. D., & Acernese, F. 2017a, ApJL, 848, L12
Abbott, B. P., Abbott, R., Abbott, T. D., et al. 2017b, ApJL, 848, L13
Abbott, B. P., Abbott, R., Abbott, T. D., et al. 2017c, PhRvL, 119, 161101
Aloy, M. A., Müller, E., Ibáñez, J. M., Martí, J. M., & MacFadyen, A. 2000, ApJL, 531, L119
Arcavi, I., Hosseinzadeh, G., Howell, D. A., et al. 2017, Natur, 551, 64
Arcones, A., & Montes, F. 2011, ApJ, 731, 5
Arnett, W. D. 1980, ApJ, 237, 541
Arnett, W. D. 1982, ApJ, 253, 785
Barbarino, C., Sollerman, J., Taddia, F., et al. 2021, A&A, 651, A81
Barnes, J. 2020, FrP, 8, 355
Barnes, J., Duffell, P. C., Liu, Y., et al. 2018, ApJ, 860, 38
Barnes, J., & Kasen, D. 2013, ApJ, 775, 18
Barnes, J., Kasen, D., Wu, M.-R., & Martínez-Pinedo, G. 2016, ApJ, 829, 110
Barnes, J., Zhu, Y. L., Lund, K. A., et al. 2021, ApJ, 918, 44
Bartos, I., & Márka, S. 2019, ApJL, 881, L4
Bauswein, A., Goriely, S., & Janka, H.-T. 2013, ApJ, 773, 78
Beloborodov, A. M. 2003, ApJ, 588, 931
Beniamini, P., Dvorkin, I., & Silk, J. 2018, MNRAS, 478, 1994
Beniamini, P., Hotokezaka, K., & Piran, T. 2016, ApJL, 829, L13
Berger, E. 2014, ARA&A, 52, 43
Bianco, F. B., Modjaz, M., Hicken, M., et al. 2014, ApJS, 213, 19
Bloom, J. S., Kulkarni, S. R., Price, P. A., et al. 2002, ApJL, 572, L45
Bovard, L., Martin, D., Guercilena, F., et al. 2017, PhRvD, 96, 124005
Brauer, K., Ji, A. P., Drout, M. R., & Frebel, A. 2021, ApJ, 915, 81
Bromberg, O., & Tchekhovskoy, A. 2016, MNRAS, 456, 1739
Bruenn, S. W., Lentz, E. J., Hix, W. R., et al. 2016, ApJ, 818, 123
Burbidge, E. M., Burbidge, G. R., Fowler, W. A., & Hoyle, F. 1957, RvMP, 29, 547
Burrows, A., Dessart, L., Livne, E., Ott, C. D., & Murphy, J. 2007, ApJ, 664, 416
Cameron, A. G. W. 1957, AJ, 62, 9
Cano, Z., Wang, S.-Q., Dai, Z.-G., & Wu, X.-F. 2017, AdAst, 2017, 8929054
Chase, E. A., O'Connor, B., Fryer, C. L., et al. 2022, ApJ, 927, 163
Chatzopoulos, E., Wheeler, J. C., & Vinko, J. 2012, ApJ, 746, 121
Chornock, R., Berger, E., Kasen, D., et al. 2017, ApJL, 848, L19
Colgate, S. A., Petschek, A. G., & Kriese, J. T. 1980, ApJL, 237, L81
Côté, B., Eichler, M., Arcones, A., et al. 2019, ApJ, 875, 106
Coulter, D. A., Foley, R. J., Kilpatrick, C. D., et al. 2017, Sci, 358, 1556
Cowan, J. J., Sneden, C., Lawler, J. E., et al. 2021, RvMP, 93, 015002
Cowperthwaite, P. S., Berger, E., Villar, V. A., et al. 2017, ApJL, 848, L17
de los Reyes, M. A. C., Kirby, E. N., Ji, A. P., & Nuñez, E. H. 2022, ApJ, 925, 66
Deng, J., Mazzali, P. A., Maeda, K., & Nomoto, K. 2003, NuPhA, 718, 569
Drout, M. R., Piro, A. L., Shappee, B. J., et al. 2017, Sci, 358, 1570
Drout, M. R., Soderberg, A. M., Gal-Yam, A., et al. 2011, ApJ, 741, 97
Duggan, G. E., Kirby, E. N., Andrievsky, S. M., & Korotin, S. A. 2018, ApJ, 869, 50
Eichler, D., Livio, M., Piran, T., & Schramm, D. N. 1989, Natur, 340, 126
Evans, P. A., Cenko, S. B., Kennea, J. A., et al. 2017, Sci, 358, 1565
Fernández, R., & Metzger, B. D. 2013, MNRAS, 435, 502
Fernández, R., Tchekhovskoy, A., Quataert, E., Foucart, F., & Kasen, D. 2019, MNRAS, 482, 3373
Filippenko, A. V., & Chornock, R. 2002, IAUC, 7825, 1
Fontes, C. J., Fryer, C. L., Hungerford, A. L., Wollaeger, R. T., & Korobkin, O. 2020, MNRAS, 493, 4143
Fraser, J., & Schonrich, R. 2022, MNRAS, 509, 6008
Freiburghaus, C., Rosswog, S., & Thielemann, F.-K. 1999, ApJL, 525, L121
Fröhlich, C., Hauser, P., Liebendörfer, M., et al. 2006, ApJ, 637, 415
Fujibayashi, S., Kiuchi, K., Nishimura, N., Sekiguchi, Y., & Shibata, M. 2018, ApJ, 860, 64
Galama, T. J., Vreeswijk, P. M., van Paradijs, J., et al. 1998, Natur, 395, 670
Gal-Yam, A., Ofek, E. O., & Shemmer, O. 2002, MNRAS, 332, L73
Gerardy, C. L., Fesen, R. A., Nomoto, K., et al. 2002, PASJ, 54, 905
Goldstein, A., Veres, P., Burns, E., et al. 2017, ApJL, 848, L14
Gómez, G., & López, R. 2002, AJ, 123, 328
Gottlieb, O., Lalakos, A., Bromberg, O., Liska, M., & Tchekhovskoy, A. 2022, MNRAS, 510, 4962
Grichener, A., & Soker, N. 2019, ApJ, 878, 24
Grossman, D., Korobkin, O., Rosswog, S., & Piran, T. 2014, MNRAS, 439, 757
Guillochon, J., Parrent, J., Kelley, L. Z., & Margutti, R. 2017, ApJ, 835, 64
Halevi, G., & Mosta, P. 2018, MNRAS, 477, 2366
Hjorth, J., Sollerman, J., Møller, P., et al. 2003, Natur, 423, 847
Hoffman, R. D., Woosley, S. E., & Qian, Y.-Z. 1997, ApJ, 482, 951
Horowitz, C. J., Arcones, A., Cote, B., et al. 2019, JPhG, 46, 083001
Hotokezaka, K., Kiuchi, K., Kyutoku, K., et al. 2013, PhRvD, 87, 024001
Hotokezaka, K., Tanaka, M., Kato, D., & Gaigalas, G. 2021, MNRAS, 506, 5863

Hunter, D. J., Valenti, S., Kotak, R., et al. 2009, A&A, 508, 371
Janka, H.-T., Melson, T., & Summa, A. 2016, ARNPS, 66, 341
Jeon, M., Besla, G., & Bromm, V. 2021, MNRAS, 506, 1850
Jerkstrand, A. 2017, in Handbook of Supernovae, ed. A. W. Alsabti & P. Murdin (Switzerland: Springer), 795
Ji, A. P., Frebel, A., Chiti, A., & Simon, J. D. 2016, Natur, 531, 610
Just, O., Bauswein, A., Ardevol Pulpillo, R., Goriely, S., & Janka, H.-T. 2015, arXiv:1504.05448
Just, O., Goriely, S., Janka, H.-T., Nagataki, S., & Bauswein, A. 2022, MNRAS, 509, 1377
Kasen, D., Badnell, N. R., & Barnes, J. 2013, ApJ, 774, 25
Kasen, D., Metzger, B., Barnes, J., Quataert, E., & Ramirez-Ruiz, E. 2017, Natur, 551, 80
Kasliwal, M. M., Kasen, D., Lau, R. M., et al. 2022, MNRAS, 510, L7
Kasliwal, M. M., Nakar, E., Singer, L. P., et al. 2017, Sci, 358, 1559
Kilpatrick, C. D., Foley, R. J., Kasen, D., et al. 2017, Sci, 358, 1583
Korobkin, O., Rosswog, S., Arcones, A., & Winteler, C. 2012, MNRAS, 426, 1940
Kuroda, T., Arcones, A., Takiwaki, T., & Kotake, K. 2020, ApJ, 896, 102
Kyutoku, K., Ioka, K., Okawa, H., Shibata, M., & Taniguchi, K. 2015, PhRvD, 92, 044028
Lattimer, J. M., & Schramm, D. N. 1974, ApJL, 192, L145
Liljegren, S., Jerkstrand, A., Barklem, P. S., et al. 2022, arXiv:2203.07021
Lourie, N. P., Baker, J. W., Burruss, R. S., et al. 2020, Proc. SPIE, 11447, 114479K
MacFadyen, A. I., & Woosley, S. E. 1999, ApJ, 524, 262
Macias, P., & Ramirez-Ruiz, E. 2019, ApJL, 877, L24
Madison, D., & Li, W. 2007, CBET, 1034, 1
Maeda, K., Mazzali, P. A., Deng, J., et al. 2003, ApJ, 593, 931
Maeda, K., Nakamura, T., Nomoto, K., et al. 2002, ApJ, 565, 405
Mazzali, P. A., Deng, J., Maeda, K., et al. 2002, ApJL, 572, L61
Mazzali, P. A., Deng, J., Tominaga, N., et al. 2003, ApJL, 599, L95
McCully, C., Hiramatsu, D., Howell, D. A., et al. 2017, ApJL, 848, L32
Meikle, P., Lucy, L., Smartt, S., et al. 2002, IAUC, 7811, 2
Metzger, B. D., Martínez-Pinedo, G., Darbha, S., et al. 2010, MNRAS, 406, 2650
Metzger, B. D., Piro, A. L., & Quataert, E. 2008, MNRAS, 390, 781
Metzger, B. D., Thompson, T. A., & Quataert, E. 2007, ApJ, 659, 561
Meyer, B. S., & Brown, J. S. 1997, ApJS, 112, 199
Miller, J. M., Sprouse, T. M., Fryer, C. L., et al. 2020, ApJ, 902, 66
Modjaz, M., Liu, Y. Q., Bianco, F. B., & Graur, O. 2016, ApJ, 832, 108
Molero, M., Romano, D., Reichert, M., et al. 2021, MNRAS, 505, 2913
Mösta, P., Richers, S., Ott, C. D., et al. 2014, ApJL, 785, L29
Mösta, P., Roberts, L. F., Halevi, G., et al. 2018, ApJ, 864, 171
Müller, B., Melson, T., Heger, A., & Janka, H.-T. 2017, MNRAS, 472, 491
Mutchler, M., Bellini, A., Casertano, S., et al. 2021, BAAS, 53, 2021n6i216p01
Naidu, R. P., Ji, A. P., Conroy, C., et al. 2022, ApJL, 926, L36

Nakar, E. 2007, PhR, 442, 166
Nicholl, M., Berger, E., Kasen, D., et al. 2017, ApJL, 848, L18
Perego, A., Rosswog, S., Cabezón, R. M., et al. 2014, MNRAS, 443, 3134
Perley, D. A., Fremling, C., Sollerman, J., et al. 2020, ApJ, 904, 35
Prentice, S. J., Ashall, C., James, P. A., et al. 2019, MNRAS, 485, 1559
Qian, Y., & Woosley, S. E. 1996, ApJ, 471, 331
Radice, D., Perego, A., Hotokezaka, K., et al. 2018, ApJ, 869, 130
Scheck, L., Kifonidis, K., Janka, H. T., & Müller, E. 2006, A&A, 457, 963
Schönrich, R. A., & Weinberg, D. H. 2019, MNRAS, 487, 580
Shappee, B. J., Simon, J. D., Drout, M. R., et al. 2017, Sci, 358, 1574
Siegel, D. M. 2019, EPJA, 55, 203
Siegel, D. M., Agarwal, A., Barnes, J., et al. 2021, arXiv:2111.03094
Siegel, D. M., Barnes, J., & Metzger, B. D. 2019, Natur, 569, 241
Siegel, D. M., & Metzger, B. D. 2017, PhRvL, 119, 231102
Smartt, S. J., Chen, T. W., Jerkstrand, A., et al. 2017, Natur, 551, 75
Soares-Santos, M., Holz, D. E., Annis, J., et al. 2017, ApJL, 848, L16
Stanek, K. Z., Matheson, T., Garnavich, P. M., et al. 2003, ApJL, 591, L17
Surman, R., & McLaughlin, G. C. 2004, ApJ, 603, 611
Symbalisty, E., & Schramm, D. N. 1982, ApJL, 22, 143
Szalai, T., Zsíros, S., Fox, O. D., Pejcha, O., & Müller, T. 2019, ApJS, 241, 38
Taddia, F., Sollerman, J., Fremling, C., et al. 2019, A&A, 621, A71
Tanaka, M., & Hotokezaka, K. 2013, ApJ, 775, 113
Tanaka, M., Kato, D., Gaigalas, G., & Kawaguchi, K. 2020, MNRAS, 496, 1369
Tanaka, M., Kawabata, K. S., Maeda, K., Hattori, T., & Nomoto, K. 2008, ApJ, 689, 1191
Tanaka, M., Utsumi, Y., Mazzali, P. A., et al. 2017, PASJ, 69, 102
Tanvir, N. R., Levan, A. J., González-Fernández, C., et al. 2017, ApJL, 848, L27
Taubenberger, S., Valenti, S., Benetti, S., et al. 2009, MNRAS, 397, 677
Thielemann, F.-K., Wehmeyer, B., & Wu, M.-R. 2020, JPhCS, 1668, 012044
Thompson, T. A., Burrows, A., & Meyer, B. S. 2001, ApJ, 562, 887
Thompson, T. A., Chang, P., & Quataert, E. 2004, ApJ, 611, 380
Thompson, T. A., & ud-Doula, A. 2018, MNRAS, 476, 5502
Tomita, H., Deng, J., Maeda, K., et al. 2006, ApJ, 644, 400
Tsujimoto, T. 2021, ApJL, 920, L32
van de Voort, F., Pakmor, R., Grand, R. J. J., et al. 2020, MNRAS, 494, 4867
Villar, V. A., Cowperthwaite, P. S., Berger, E., et al. 2018, ApJL, 862, L11
Vlasov, A. D., Metzger, B. D., Lippuner, J., Roberts, L. F., & Thompson, T. A. 2017, MNRAS, 468, 1522
Waxman, E., Ofek, E. O., Kushnir, D., & Gal-Yam, A. 2018, MNRAS, 481, 3423
Winteler, C., Käppeli, R., Perego, A., et al. 2012, ApJL, 750, L22
Woosley, S. E., & Bloom, J. S. 2006, ARA&A, 44, 507
Yoon, S.-C., Chun, W., Tolstov, A., Blinnikov, S., & Dessart, L. 2019, ApJ, 872, 174
Yoshii, Y., Tomita, H., Kobayashi, Y., et al. 2003, ApJ, 592, 467
Zevin, M., Kremer, K., Siegel, D. M., et al. 2019, ApJ, 886, 4